Research Square

Preprints are preliminary reports that have not undergone peer review.
They should not be considered conclusive, used to inform clinical practice,
or referenced by the media as validated information.

The 2020 Khoy–Qotour (NW Iran) earthquake sequence reveals strain partitioning and suture-zone fragmentation during Arabia–Eurasia convergence

Mustafa Toker

tokermu@gmail.com

Yuzuncu Yıl University

Evrim Yavuz

Istanbul Metropolitan Municipality

Murat Utkucu

Sakarya University

Duygu Akçay

Kocaeli Üniversitesi

Fadime Sertçelik

Kocaeli Üniversitesi

Research Article

Keywords: NW-Iran, E-Anatolia, Seismology, CMT: Co-seismic stress, Pull-apart, tensor inversion

Posted Date: November 20th, 2026

DOI: https://doi.org/10.21203/rs.3.rs-10867696/v1

License: This work is licensed under a Creative Commons Attribution 4.0 International License.
Read Full License

Additional Declarations:
No competing interests reported.

Tables 1 to 3 are available in the Supplementary Files section.

The 2020 Khoy–Qotour (NW Iran) earthquake sequence reveals strain partitioning and suture-zone fragmentation during Arabia–Eurasia convergence

Mustafa Toker[1*], Evrim Yavuz[2], Murat Utkucu[3,4], Duygu Akçay[5], Fadime Sertçelik[5]

Yuzuncu Yıl University[1*], Department of Geophysical Engineering, Van, Turkey
Istanbul Metropolitan Municipality[2], Directorate of Earthquake and Geotechnical Investigation, İstanbul Turkey
Sakarya University[3], Department of Geophysical Engineering, Sakarya, Turkey
Sakarya University[4], Disaster Management Application and Research Center, Sakarya, Turkey
Kocaeli University[5], Department of Geophysical Engineering, Kocaeli, Turkey.

Corresponding author[*]:

Dr. Mustafa Toker

Yuzuncu Yıl University,

Faculty of Engineering,

Department of Geophysical Engineering,

Van (Turkey)

Mobile: +90 (543) 624 75 03

E-mail: tokermu@gmail.com

Abstract

The 23 February 2020 Khoy–Qotour earthquake sequence (Mw 5.6 and Mw 5.8) occurred within the Neotethyan Suture Zone (NTS) along the Turkey–Iran border, where the mechanisms accommodating deformation associated with the Arabia–Eurasia collision remain poorly constrained. We integrate double-difference earthquake relocation, centroid moment tensor (CMT) solutions, Coulomb stress transfer analysis, Sentinel-1A, D-InSAR observations, and regional stress tensor inversion to investigate rupture evolution, strain partitioning, and their geodynamic significance. The first mainshock ruptured a N–S-striking normal fault, whereas the second ruptured a NW–SE-striking right-lateral strike-slip fault at a depth of ~8 km. Relocated seismicity and focal mechanisms demonstrate that the earthquake sequence developed within an upper-crustal zone where normal and strike-slip faulting coexist and interact. Coulomb stress modelling indicates that the first rupture promoted failure on adjacent strike-slip and normal faults, producing a NW–SE-trending zone of stress increase and seismic activation at depths of 6–11 km, together with a W–E-oriented stress shadow characterized by aseismic stress release between 6 and 8 km. Stress tensor inversion, consistent with focal mechanisms and geodetic deformation, defines an extensional strike-slip regime under NNW–SSE maximum horizontal compression. The combined seismological and geodetic observations indicate that deformation was accommodated by coupled normal and strike-slip faulting within a pull-apart system, promoting oblique upper-crustal extrusion toward the WNW. We propose that this earthquake sequence records active strain partitioning within the NTS zone, where inherited structures localize transtensional deformation and facilitate progressive fragmentation of the suture between the E-Anatolian and NW-Iranian blocks. These findings provide new constraints on how oblique Arabia–Eurasia convergence is partitioned within continental collision zones and highlight the role of inherited suture-zone structures in controlling earthquake rupture and crustal deformation.

Key words: NW-Iran; E-Anatolia; Seismology; CMT: Co-seismic stress; Pull-apart; tensor inversion.

1. Introduction

The 5.6 *M*w Khoy-Qotour earthquake occurred at 05:53 UTC on February 23, 2020, in Khoy county in the Qotur district on the border between Iran and Turkey, in the N of W-Azarbaijan province in NW-Iran (Fig. 1a) (Taymaz et al., 2022; Rezapour, 2024). The epicenter was 115 km from Urmia, 168 km from Tabriz and 2 km from Qotur, at a shallow depth of 8 km, according to the Iranian Seismological Center (IRSC). Subsequently, around 10 hours later, a second, somewhat bigger, 5.8 *M*w, earthquake occurred at 16:00 UTC with the epicenter again at a depth of 8 km (Figs. 1a, b). The close spatio-temporal relationship of the first mainshock (designated Khoy 1, or K1) and the second mainshock (Khoy 2, or K2), together with their comparable magnitudes justify treating them as consecutive earthquakes (Fig. 1c). These consecutive mainshocks were followed by a series of many equivalent magnitude and/or similar sized aftershock events. Relatively strong consecutive K1 and K2 quakes rocked both the Qotur and Khoy areas and seriously damaged dozens of villages and ~4500 buildings, injuring ~200 people and killing ~10 people (AFAD, 2020; KOERI, 2020), while communications and the power network within the quake-hit region was severely disrupted (IRSC).

The initial locations of the K1 and K2 events computed immediately after the earthquakes indicated that the two events occurred in a narrowing zone of Neotethyan suture (NTS) (Fig. 1a), bounded by a conjugate of the NW-SE striking right-lateral, segmented Saray Fault Zone (SFZ) and the NE-SW striking left-lateral Baskale Fault (BF) strike-slip features (Figs. 1b, c, MTA, 2022). Furthermore, these earthquakes happened in an area of low deformation and flanked by deep-seated faults, such as Guilato-Siahcheshmeh-Khoy fault (GSKF), making up the N portion of the North Tabriz Fault (NTF) (Hessami et al. 2003; Cisternas and Philip 1997; Reilinger et al. 2006; Djamour et al. 2011; Ghods et al., 2015) (Fig. 1a). The faults asymmetrically ruptured at the SE-end of the SFZ, near the NE-end of the BF, have mostly extensional and right-lateral strike-slip faulting features, with source duration between 24 s (K1) and 31 s (K2), reported by national agencies (TMMOB, 2020), and with estimated co-seismic slip of ~30 cm (max) and vertical displacement of ~10-15 cm (max) in this study. This pair of consecutive quakes offers an excellent example of a spatio-temporal earthquake pattern. However, the question of the partitioning of the deformation in the active intraplate setting of the Arabia-Eurasia convergence remains a major issue in tectonics. Furthermore, the suggestion of stress transfer among neighboring fault segments and multiple simultaneous

ruptures, similar to the 1780 and 1786 earthquakes in NTF (Berberian, 1976, 1997; Berberian and Yeats, 1999), implies a progressive nature of these two events (Stein and Lisowski, 1983; Stein et al., 1992).

In active intraplate settings, crustal deformation is commonly focused in the borders of 'rhomb-shaped blocks' so that these blocks undergo minimal internal deformation (Taylor and Peltzer 2006; Ghods et al., 2015). The K1 and K2 events occurred within such a cryptic and complex area of the NTS, where the Muş suture (MS), the GSKF and the Main Recent Fault (MRF in Zagros) unevenly dissipate (see Fig. 1a). The precise relationship between the relatively small scale strike-slip SFZ and BF and the large scale collisional features, for example the NTS and MRF, is unknown. However, elucidating this mechanism of regional N-S shortening and E-W extension in the E-Anatolian and the NW-Iranian regions is key to understanding how the Arabia-Eurasia collision is accommodated (Copley and Jackson, 2006; Berberian, 1997; Berberian and Yeats, 1999; Karakhanian et al., 2004; Berberian, 2014).

Readers may ask, why are these two earthquakes the focus of this study? Initially derived fault focal solutions from the first motion analyses, performed in this study, have revealed nearly dominant extensional and strike-slip deformations along the small-scale SFZ and BF, respectively, within the large scale NTS (Figs. 1a-c). This implies that the conversion of strike-slip into normal-slip motion, together with crustal extension along the SFZ and BF, accommodated the N-S compression, affecting both the E-Anatolia and NW-Iranian regions. This observation is very unusual seismologically but may have implications for other complex areas in the region (e.g., Lakes Van and Erçek in Toker and Şahin, 2022) (Fig. 1a). However, in E-Anatolia and NW-Iran, the lack of emphasis on nearly pure extensional and strike-slip aspects is surprising, given the existence of numerous extensional faults and related basins (Dhont and Chorowicz, 2006; Toker et al., 2017a, b; Toker and Tur, 2018; Toker and Şahin, 2019; Toker et al., 2021; Solaymani Azad et al., 2015; Ghods et al., 2015; Yesilova et al., 2019, 2021) and the theoretical seismic link between extension, strike-slip deformation and earthquakes (e.g., Toker et al., 2017b, 2021). Unfortunately, this seismic behavior and the seismotectonic characteristics have largely been ignored, particularly within large extensional areas of E Anatolia, such as Lakes Van and Erçek basins, the Baskale faulted basin by Yesilova, 2021, 2022 and the NTS zone (Fig. 1a). This study will examine and attempt to better understand these issues.

In the absence of large-scale, continuous faults in the E-Anatolian and NW-Iranian regions (Solaymani Azad et al., 2015, 2019; Ghods et al., 2015), interseismic strain accumulation may be expressed through intraplate, small-scale discontinuous faults. Moreover, relatively minor strain features may arise and grow across collisional areas, for example across the NTS, but may only be activated rarely. A grouping of small-scale right-/left-lateral strike-slip faults, on the SFZ and BF, respectively, are probably involved in accommodating a disproportionate degree of interseismic deformation, both in E-Anatolia and NW-Iran (Fig. 1a). Both forms of the lateral strike-slip motion appear to transition into crustal-scale extensional shear zones in order to accommodate stress related to the Arabia-Eurasia collision, although this has not been explained until now. Specifically, we sought to determine the partitioning pattern of crustal strains, which are accommodated within a block-like zone bordered by the active SFZ and BF crustal faults and investigate whether the consecutive mainshocks were due to reactivation of pre-existing structural weaknesses, perhaps in the faults and/or basement. Lastly, we relate this unexpected pair of K1 and K2 events to the geodynamic framework of the E-Anatolian and NW-Iranian blocks, associated with NTS fragmentation and separation. In this context, a detailed geophysical analysis was necessary to improve current understanding of the continental deformation and regional seismic hazard in E-Anatolia and NW-Iran, and thus in similar regions elsewhere.

The study analyses, incorporating different but mutually supportive approaches, were designed to investigate several features of the K1 and K2 events. The first aim was to derive fault source mechanisms of the two mainshocks-aftershock sequence, general knowledge of the main faulting styles of ruptures and major deformation characteristics of all the located events, associated with Coulomb failure stress changes estimated for every location. The second aim was to observe co-seismic surface deformation patterns of ruptured source faults associated with aftershock focal mechanisms. The third aim was to identify the direction of the maximum main horizontal stress, together with the main tectonic stress regime associated with focal mechanisms and compiled focal data. The final objective was to develop a properly designed, appropriate tectonic deformation model by combining all these results, estimated by each of the applied methods, and compare this with data from previously reported observations in and around the study area.

In order to achieve these aims, we will apply a series of “seismo-geodetic” analytical methods to the earthquake data set to constrain “strain partition”, extension and strike-slip division of

the Arabia-Eurasia convergence and the possible fragmentation and separation in and along the E-section of the NTS (Fig. 1a). This resulted in improved constraint of the seismic behavior of the conjugate SFZ and BF faults, and thus improved assessment of the seismic hazard for the study area and surroundings (Figs. 1b, c). These results may also help increase the general understanding of extensional and strike-slip deformation in and along small-scale conjugate faults in active collision zones, and the current geodynamics of the Turkish-Iranian High Plateau (TIHP) (Soleymani Azad et al., 2015, 2019; Aflaki et al., 2021; Niassarifard et al., 2021; Toker and Pınar, 2024). We believe the results of our systematic analyses will complement those of earlier geodynamic and geophysical studies in the study area and its close surroundings, including Lakes Van and Erçek areas (Koulakov et al., 2012; Rolland, 2017; Reid et al., 2019; Artemieva and Shulgin, 2019; Mahatsente et al., 2018; Delph et al., 2015; Toker and Tur, 2018, 2021; Toker and Şahin, 2019; Toker et al., 2017a, b; Toker et al., 2021; Toker and Şahin, 2022; Toker and Pınar, 2024).

This study will examine several topics in subsequent sections. The first is the regional seismicity and tectonic background of the K1 and K2 earthquakes, derived from previous research. Secondly, fault source mechanisms and focal solutions of all located events will be investigated using regional data. The third topic will be computation of the co-seismic stress changes and stress transfer for every observed event. Fourthly, we will discuss the co-seismic surface deformation patterns of ruptured faults. The fifth topic will be the main tectonic stress regime estimated for the study area. Finally, we will outline a tectonic model of faulting styles related to crustal deformations on the conjugate SFZ and BF faults, taking into account all the available data.

2. Seismotectonic setting

The region incorporating E-Anatolia and NW-Iran, the TIHP (Fig. 1a), came into being because of the N-motion of the Arabian plate into the Eurasian plate and exhibits active and complex faulting, fold development above blind thrusts, dense volcanic activity (Copley and Jackson, 2006), and landscape features with significant altitude, similar to the Alpine or Himalayan mountains (Jackson and Ambraseys, 1997; Jackson, 1992; Jackson and McKenzie, 1984). The evident large-scale topography and regional surface morphology are a result of two mechanisms; the Eocene to Miocene collision and the continuing Arabian/Eurasian convergence (Solaymani Azad et al., 2015; Shirzad et al., 2024; Mohammed et al., 2023). The

current estimate of the motion of the Arabian plate in terms of the Eurasian plate is ~20 to 25 mm yr^{-1} (Nilforoushan et al., 2003; Vernant et al., 2004; Solaymani Azad et al., 2015).

E-Anatolia is bounded by three Neotethyan sutures in the Northern section, Southern section and Eastern section. These are the İzmir-Ankara-Erzincan suture (IAES) in the N, the Bitlis Zagros suture (BZS) in the S and Neotethyan suture (NTS) in the E (Fig. 1a), as compiled from Topuz et al., (2017). The NTS in the E is the less well-known boundary between E-Anatolia and NW-Iran (Toker and Pınar, 2024 and references therein). The NTS, which is actively deformed by parallel/sub-parallel right-lateral strike-slip fault segments, diffused extensional fault systems and complex extensional fractures toward NNW, appears as a broadly widening shear zone, subparallel to the GSKF segment of the NTF, and is a main earthquake source, for example the Chalderan fault (CF in Fig. 1a) between the E-Anatolian and NW-Iranian blocks. The NTS zone may be interpreted to be the Eastern Caucasus-Western Iran Boundary (ECWIB), a major tectonic boundary (Rolland, 2017), which is a reactivated, dextral transform fault (see Rolland, 2017 for the location; Toker and Pınar, 2024). E-Anatolia is characterized by intense diffuse deformation and a series of short, discontinuous NE-SW and NW-SE-trending conjugate strike-slip fault segments (Fig. 1a), while the Anatolian plate is also flanked by conjugate strike-slip faults, the East Anatolian Fault Zone (EAFZ) and the North Anatolian Fault Zone (NAFZ), and extrudes laterally westward. Tomographic imaging of the upper mantle has revealed the presence of high velocity domains within more widespread low-velocity features; these have been interpreted as parts of the detached slab (Skobeltsyn et al., 2014; Toker and Şahin, 2019, 2022; Toker and Pınar, 2024). Seismicity, which is mostly related to strike-/oblique-slip and reverse faulting at shallow depths (Örgülü et al., 2003; Toker et al., 2017b, 2021), is prominently clustered in the seismically highly active Lakes Van and Erçek regions and surrounds, further to the E (SFZ and BF) (Figs. 1b, c) (Toker and Pınar, 2024).

Crustal deformation occurring after the late Miocene in NW Iran has been largely due to N-S shortening in conjunction with E-W extension (Berberian, 1981, 1997; Berberian and Yeats, 1999; Berberian, 2014; Cisternas and Philip, 1997; Copley and Jackson, 2006; Karakhanian et al., 2004; Shirzad et al., 2024; Mohammed et al., 2023). In NW Iran, much of the right-lateral strike-slip movement occurs in the NTF, and the GSKF system (Fig. 1a) (Salmanian et al., 2025). The NW–SE striking NTF has been interpreted as a extension of the GSKF to the east (Berberian, 1997; Karakhanian et al., 2004; Solaymani Azad et al., 2015). The current slip in

the NTF is approximately 5-8 mm yr^{-1} (Masson et al., 2006; Vernant and Chéry, 2006; Rizza et al., 2013), which is greater than the estimates of geological slip (~2 mm yr^{-1}) in the Holocene in the NW section of the NTF (Karakhanian et al., 2004; Solaymani Azad et al., 2015). The northern termination of the GSKF (GSKF-1) has what has been described as a "horsetail" geometry. This is composed of small N-S normal faults, sections with right-/left-lateral parallel/sub-parallel strike-slip faults and complex folded structures, associated with numerous active volcanoes with extensional fissures/fractures (Solaymani Azad et al., 2015; Salmanian et al., 2025 and references therein) (Fig. 1a). These horsetail features, dispersed in a zone of the NTS, accommodate block extrusion in NW-Iran toward the E. The GSKF comprises a faulting system, positioned between two opposite extensional and compressional tectonic regimes, and consistent with the N-S convergence of the Arabian and Eurasian plates (Solaymani Azad et al., 2015, 2019; Aflaki et al., 2021; Shirzad et al., 2024; Mohammed et al., 2023).

The TIHP has historically experienced large and destructive earthquakes (Berberian, 1997; Berberian and Yeats, 1999; Karakhanian et al., 2004; Berberian, 2014; Cisternas and Philip, 1997; Solaymani Azad et al., 2015) (Fig. 1a). Most of the earthquake foci have been shallow (Siahkali Moradi et al., 2011) and there is often accompanying surface faulting (Berberian and Yeats, 1999; Hessami et al., 2003a; Karakhanian et al., 2004; Solaymani Azad et al., 2015). These strong earthquakes, usually associated with large magnitudes, long recurrence intervals and periods of high activity, that is temporal seismic clustering, have been interpreted as typical intraplate events (Berberian and Yeats, 1999; Solaymani Azad et al., 2015). The tectonic deformation is almost totally accommodated by co-seismic slip, as implied by measurement of earthquake-related seismic moment in E-Anatolia and NW-Iran, (Jackson and Ambraseys, 1997; Solaymani Azad et al., 2015). In the last 90 years seismicity in NW-Iran has mostly been associated with the NTF (Ghods et al., 2015; Salmanian et al., 2025), which was also the site of two catastrophic earthquakes in the 18th century (Ambraseys and Melville 1982). Previous studies have suggested that the NTF may have generated M >7.5 earthquakes, but there have been no earthquakes of M >7.0 in the past 235 years (Berberian, 1997). Most recently, the 11 August 2012 doublet earthquake (Mw 6.4 and 6.3) occurred on the NTF, causing >300 deaths and 3000 injuries (Copley et al., 2013). Historically, five destructive earthquakes (from the earliest, Sarab in 1593, progressing through the SE-Tabriz in 1721, NW-Tabriz in 1780 and the Marand in 1786 to the Tassuj in 1807, has shown a seismic migration from the SE to the NW (GSKF-2) over a period of 214 years (Solaymani

Azad et al., 2015). This has been described as earthquake clustering (Berberian, 1997; Kagan and Jackson, 1991; Karakhanian et al., 2004) and attributed to interactions between NTF structural faults (Solaymani Azad et al., 2015) (Fig. 1a). Recent studies of the NTF have found many shallow (7-21 km) microseismic events (Siahkali Moradi, 2008; Siahkali Moradi et al., 2011; Solaymani Azad et al., 2015).

3. Data and Methods

3.1. Relocations

Following the K1 and K2 mainshocks, around 55 aftershocks ($3.0 < Mw < 4.9$) were initially located using the catalogs of the General Directorate of Disaster Affairs of Turkey (AFAD), and Bogazici University, Kandilli Observatory (KOERI) Regional Earthquake-Tsunami Monitoring Center (BDTIM) (Fig. 1d), while ~200 small events ($Mw < 3.0$) were removed from the initial location procedure. Manual selection of P- and S-wave arrival times was performed using the recorded seismograms and phase readings were carefully merged for the events involved in both catalogs (AFAD and KOERI). The events with more than five P- and three S-wave arrival-time readings were included in the combined catalog. The phase selections for the events with magnitudes ≥ 3.5 were revised using continuous waveforms during the aftershock sequence. The final combined record contained 34 events, including both mainshocks, located by the program Hypo71 (Lee and Lahr, 1972) between 2012 and 2020 and both P-wave and S-wave phase readings.

Initial locations obtained from Hypo71 using the 1-D velocity model (Kalafat et al., 1987) (Table 1) are shown in Fig. 2a. The mean horizontal errors (EH) of the relocated events ranged between ~1.0 to ~4.9 km, while the mean vertical errors (EZ) ranged between ~0.2 to ~0.8 km. The azimuthal gap varied between 180° and 270° for most of the events and the root mean square (RMS) of the events ranged between 0.36 s and 0.89 s. Initial locations from Hypo71 were further improved to make the locations more reliable using a different algorithm, the double-difference earthquake, relative location algorithm HypoDD (Waldhauser and Ellsworth, 2000; Waldhauser, 2001). The relocations using HypoDD are shown in Fig. 2a and the relative errors (EX, EY, EZ and RMS) after HypoDD processing are presented in Fig. S1. In Fig. S1, the EX and EY, equivalent to EH with Hypo71, ranged from ~0.2 to ~3.6 km, while the EZ ranged from ~0.2 to ~2.9 km. However, the EZ of 23/34 (79%)

events was less than ~0.6 km and the RMS ranged from ~0.54 s to ~0.96 s. Due to unbalanced station coverage, the relocation analysis suffered from location bias. Additional data obtained from the International Seismological Centre (ISC) are thus included to perform and improve the locations, with the small ISC catalog azimuthal gaps (ISC, 2022 and see Bondâr and Storchak, 2011 for improved location procedure). Of the 132 aftershocks (Mw ≥ 3.0), including the initial 34 events, retrieved from the ISC bulletin are located and shown in Fig. 2a, and a table listing the final locations is shown in Table S1. As seen in Fig. S1, ~75% of the final ISC locations had acceptable azimuthal gaps of ≤ 80º. Comparison of the locations obtained from Hypo71 and HypoDD showed more diffuse distribution, while the ISC locations yielded a relatively more compact clusteral pattern of distribution of the events, as shown in Fig. 2a.

3.2. Centroid Moment Tensor (CMT) Inversion

Data from stations > 400 km distant were disregarded for regional inversion analysis. We chose to do this mainly because of regional tectonic heterogeneity and because of increasing discrepancies between observed and derived waveforms at large distances during early tests. For both mainshocks and the aftershocks, the number of stations used was either 5 or 8, while from 10 to 24 waveforms were used. The data from a total of 22 earthquakes were retrieved from KOERI for CMT inversion, ranging in magnitude from Mw 3.9-Mw 5.9, using full waveform CMT inversion, horizontal and vertical components of P-, S-waves and three-components of the surface waves. Before inversion, a band-pass filter of 0.02-0.09 Hz was applied for each event, as we have previously described (Toker et al, 2023). The frequency-wavenumber algorithm of Bouchon (1981) was used to compute Green's functions using the 1-D crustal velocity model of Kalafat et al. (1987) (Table 1).

We used the ISOLA inversion method for the best-fitting focal mechanism solutions and selected the optimal double-couple (DC) mechanism and moment magnitude. The main function of the ISOLA algorithm, a MATLAB-based interface, is similar to the Kikuchi and Kanamori (1991) iterative inversion approach. With the ISOLA algorithm, local, regional and teleseismic events of Mw >3.5 may be subjected to waveform inversion analysis. This algorithm has been used to analyze source mechanisms of small and moderately sized events, using both regional surface and body waves, employing a grid search technique to estimate source parameters.

Source locations were estimated by iterating the moment tensor linear inverse solution. Thus, the most likely centroid depths are identified using the grid-search varying from 5 to 25 km, with a 1 km grid spacing. The grid with the best absolute value correlation coefficient between observed and theoretical (real-world measurement and computed) seismograms will yield the source location. This best fit value is termed the variance reduction (VR) (the algorithm by Sokos and Zahradnik, 2008, 2013). In addition to VR, a number of corresponding inversion metrics are also taken into account. These include the signal-to-noise ratio (SNR), DC ratio (%), the condition number (CN), while the space-time variability (STVAR) and focal mechanism variability (FMVAR) index are simultaneously performed to investigate the accuracy and robustness of the inversion solution. The CMT inversion results are shown in Fig. 2b and the related source parameters are given in Table 2. Two poorly-resolved aftershocks, with a VR lower than 50% (0.41 to 0.47), were retained (Table 2) due to their large DC% component, together with the 20 well-constrained aftershocks with >50% VR (0.55-0.79).

Inversion resulted in good constraint for 22 of the 34 events (Table 2) and robust solutions were obtained for the remaining source parameters (Fig. 2b). Of note, all the events subjected to analysis occurred at shallow centroid depths from about 5 to 12 km with an error of ±2 km. These findings were inconsistent with the initial relocations obtained from both the Hypo71 and HypoDD algorithms (Fig. 2a). For interpretation of the data, we preferred to use the well-constrained centroid depths, rather than estimates from relocated hypocenters (EZ) by HypoDD. An example solution, shown in Fig. S2, illustrates selected events (#8, 13, 17, Table 2). We plotted correlation against depth for strike, dip and rake obtained from the grid search. This provided an best-fit estimate of area with well-constrained centroid depth. Furthermore, additional illustrations of waveform fitting, together with centroid depth grid-search results, constrained for both the K1, K2 mainshocks and one independent event (#3, 5, 9, Table 2), are shown in Fig. S3. In Figs. S2 and S3, correlation vs focal depth plots for the CMT solutions suggest that the focal mechanisms were not stable between depths of 3-5 km (low correlation), but more stable at depths of 6-9 km (high correlation). This is due to a sudden velocity decrease in the long-period S-wave at the first 5 km depth (Table 1).

In order to validate the obtained mainshock and aftershock solutions, we compared them with the equivalent data in the Global CMT catalog (GCMT). Fig. 2b illustrates such an evaluation of the four focal mechanisms that were common in our data and the GCMT. Only four of

them appeared the same and/or similar (#1, 5, 9, 14), taking focal mechanisms and orientation of the fault into consideration. Only three of a total of seven events (#23, 24, 25 in Fig. 2b, Table 2) have completely different and independent mechanisms, which are strike-slip, reverse oblique-slip and normal-slip focal mechanisms, respectively. However, the two events (#23, 25) are closely consistent with other strike-slip and normal focal mechanisms evident in the study area, supporting our faulting regime.

Finally, we also constrained single source (SSS) and double source solutions (DSS) for the K1 (#5) and K2 (#9) mainshocks using teleseismic point-source inversion to again validate the focal solutions derived through regional CMT inversion (e.g., #5, 9 in Fig. S3). Teleseismic data, method and inversion details with the SSS- and DSS-modeling results are provided in S4 and shown in Fig. S4. In Fig. S4, the SSS- and DSS-modeling results for K1 suggest a centroid depth of 8 km. However, the SSS-modeling result for K2 suggests a centroid depth of 12 km, while the DSS-modeling result for K2 suggests centroid depths of 6 km and 12 km. Teleseismic point-source inversion results in Fig. S4 show that fault source parameters and focal mechanisms of the two mainshocks were closely consistent with those obtained from regional CMT inversion in Fig. S3, again supporting our faulting regime with a depth range error of ± 2 km and fault source parameters and focal solutions estimated by Taymaz et al., (2022) in the same area.

3.3. Coulomb failure stress changes

Estimating the Coulomb failure stress changes for each of the aftershocks (Fig. 2b, Table 2) and related fault parameters was performed to explore if these were consistent with the static stress changes due to the co-seismic slip of both mainshocks. This was essential to understand and interpret the nodal planes of aftershocks and ruptures, the time-dependent delay of the triggered events and the disposition of the activated faults, in and around the co-seismic slip areas of both mainshocks.

Coulomb stress failure change maps can be used to study relationships between the mainshock ruptures and following aftershocks (King et al., 1994; Harris, 1998; Stein, 1999).

Coulomb failure stress change ($\Delta\sigma_f$) may be derived using:

$$\Delta\sigma_f = \Delta\tau + \mu' \Delta\sigma_n \quad (1)$$

where $\Delta\tau$ and $\Delta\sigma_n$ represent changes in shear and normal stress, respectively (King et al. 1994; Harris, 1998). The value for the apparent coefficient of friction (μ') varied from 0.2-0.8, including the effect of pore fluid pressure variation, as previously suggested (Stein, 1999). We adopted the assumptions and method of Okada (1992) for calculating elastic dislocation resulting from co-seismic faulting, which include earthquake ruptures represented by rectangular dislocation surfaces in an elastic half-space with Young's modulus of 8 x 10^5 bar, Poisson's ratio of 0.25 and μ'=0.4.

The Coulomb stress failure accommodates changes in both shear and normal stress at the receiver fault(s) (Toda et al., 2005; Jordan et al., 2011). This can be also described as "earthquake-mediated fault interaction" (Jordan et al., 2011), in which the stress changes on the receiver fault(s) are a result of both dynamic (rupture-sourced seismicity) and quasi-static interaction from permanent source fault displacement (Gomberg et al., 2003; Jordan et al., 2011). This results in increased shear stress in the direction of the fault slip, facilitating fault failure but a concurrent increase in normal stress through the surface of the fault increases frictional strength, tending to prevent fault failure (Jordan et al., 2011). The increases in stress are dependent on several factors including the total co-seismic slip, separation distance between source and receiver faults, the relative orientation of the faults, and interaction between pore pressure and normal stress (Cocco and Rice, 2002; Jordan et al., 2011).

The source mechanisms of all locations, including the K1 and K2 mainshocks, obtained in this study (Table 2, Fig. 2b) were used to compute the stress variations using Coulomb 3.3 software (Lin and Stein, 2004; Toda et al., 2005). Here, we considered 16 representative aftershocks based on their spatial distribution and focal mechanism parameters (Fig. 2b). The locations of these proposed aftershocks, with their strike, dip and rake angles, are shown in Table 2. We selected the source parameters of the K1 event (#5, Table 2). Then, we computed Coulomb co-seismic stress variations of the K1 event over both nodal planes for each of the 16 proposed aftershocks with given source mechanisms (Table 2) to understand spatial correlations between the proposed stress changes and the aftershocks. Results are illustrated in Figs. 3-6. In Fig. 3, the stress changes are depicted at colored focals and related locations of respective aftershocks. Examples of estimated Coulomb stress change maps, depicted in Figs.

436 4-6, show unloading/loading for an event (#8) at 10 km depth (Figs. 4a, b) and
437 loading/unloading for a following event (#9) at 8 km depth (Figs. 4c, d), complete unloading
438 for two different events (#11) at 6 km depth (Figs. 5a, b) and (#17) at 8 km depth (Figs. 5c, d)
439 and complete loading for two different events (#6) at 9 km depth (Figs. 6a, b) and (#16) at 6
440 km depth (Figs. 6c, d).
441
442 In Fig. 3 and Table 2, the derived Coulomb stress changes in six of the aftershocks were
443 positive, with increases in the stress of 2 to 5 bars and both nodal planes exposed to positive
444 stress change. Seven more aftershocks underwent negative Coulomb stress changes with
445 similar magnitudes of stress decrease (2 to 5 bars) with both nodal planes experiencing
446 negative stress change. Furthermore, the stress changes in four of the proposed aftershocks
447 were both positive on one nodal plane exposed to positive stress change and also negative at
448 the other nodal plane exposed to negative stress change; in these four aftershocks the positive
449 and negative stress changes again ranged from 2-5 bars. This demonstrated that the K1
450 mainshock contributed to stress transfer, triggering and activation of these events (Fig. 3). The
451 six aftershocks in an area of increased stress with centroid depth ranging 6-11 km indicated
452 that the stress change was positive for a right lateral NW-SE trending strike-slip fault, as
453 shown in Fig. 3, coinciding with the triggered, high seismicity on the right lateral strike-
454 /oblique-slip faults (Figs. 4b, c and 6). However, the seven NW-SE striking, normal oblique-
455 /strike-slip focal mechanisms in an area of decreased stress with centroid depth ranging 6-8
456 km indicated that the stress change was also negative for a right lateral NW-SE trending
457 strike-slip fault, as shown in Fig. 3, coinciding with the reduced, low seismicity (stress
458 shadow) on the right lateral strike-/oblique-slip faults (Figs. 4a, d and 5).
459
460 These stress change estimations show that activations of the faults, with rake angles from 1°-
461 180° (Table 2), are consistent with stress transfer from the co-seismic rupture. However, the
462 magnitude of the stress changes was typically only a few bars (±5 bar) and so was markedly
463 smaller than the stress drops reported during source fault ruptures which range from 10-100
464 bars (Stein, 1999; Liu et al., 2009; Chen et al., 2010; Jordan et al., 2011).
465
466 **3.4. Co-seismic surface displacement using D-InSAR (Sentinel 1A)**
467
468 The time difference between the two earthquakes (K1 and K2), of approximately 10 hours,
469 makes it unlikely that suitable images were captured and were available. If such images

existed, albeit with a low probability, this would facilitate an independent analysis of displacements and a comprehensive interpretation of the effects caused by both earthquakes, which are thought to have triggered each other. In order to understand the situation, the image archive of the Sentinel 1A satellite chronologically as close as possible to the time of the earthquakes was examined. A time resolution and perpendicular baseline graph for possible interferograms was generated. For the selection of the interferogram to be used in analysis, all Single Look Complex (SLC) image sets with 152 (relative) orbit number in the descending mode were examined and one was selected for the period of a few hours before the K1 event; this was used as the reference image. The radar image taken 12 days after the earthquake (06.03.2021) was suitable for a differential InSAR (D-InSAR) study (Table 3).

D-InSAR analysis of the selected image pair, S1A-2020053 (reference) and S1A-2020065 (repeat) was performed through open source InSAR software, the GMTSAR program (Sandwell et al. 2011; Sandwell et al. 2016). The interferogram that represents -23 m perpendicular baseline length and 12-day time span was generated by a two-pass InSAR technique. The topographic phase was extracted from the interferogram using 1 arc-second resolution, and the SRTM1 (Farr et al. 2006) Digital Elevation Model (DEM). Fig. 7a shows the low-pass, filtered phase, interferogram overlaid onto the topography. Each fringe describes a position change of 2.8 cm in the topography along the direction line of the radar. In the interferogram (Fig. 7a) the locations of K1 and K2 are indicated by rings. The small dots represent distribution of aftershocks in the earthquake zone. As can be seen in Fig. 7a, the consecutive K1 and K2 events caused a wedge-shaped complex of multiple surface rupture propagation, with a range of ~5 to 15 km in length and NW-SE and NE-SW directions. It is thought that the largest deformation gradients in the topography occur perpendicular to these directions. Since the main deformation pattern increased from the SW to the NE (the direction of the largest gradient), but the slope of the land decreases in the same direction, it was evident that image analysis in the descending direction of the radar would be better for interpretation of resulting deformations.

The analysis performed in the ascending direction weakened the signal strength and increased its noise. For numerical evaluation of differential surface deformations on the interferogram, phase unwrap was required (see Chen and Zebker, 2000). Fig. 7b shows unwrapped phase results in millimeters (mm). The magnitudes in Line-Of-Sight (LOS) direction for each pixel have been projected on the vertical using:

$$d_{up} = \frac{d_{LOS}}{\cos \theta} \quad (2)$$

where d_{LOS} and d_{up} are LOS and vertical displacements, respectively. θ is the incidence angle of the radar. Its numerical value for each pixel was held constant at 40°. The vertical displacements over the topography, during the 12 day time span, are also displayed in Fig. 7b. Blue colors indicate that the surface has moved away from the radar, in other words, subsidence occurred. From Fig. 7b it can be inferred that a 12-15 cm block rupture occurred on the fault due to the earthquakes. Regarding the deformation distribution, the subsidence between the directions decreased its effect towards the S, as the topography increased.

To investigate the ground deformation characteristics on a profile depending on the topography, the section AA' was defined (see Fig. 7b). Fig. 7c depicts how the vertical displacement proceeded in the direction of the plane for about 70 km. The topographic height from the starting point, A, to A' decreases from 2800 m to 1300 m. The vertical rupture of approximately 20 cm on this profile occurred at the thirtieth km of AA', where the topography decreased from approximately 2800 m to 2000 m from the starting point. After 15 km from the fracture, the topography increased to 2500 m. A second fracture of approximately 5 cm was evident at the fiftieth km of the AA' section.

3.5. Stress Tensor Inversion

The focal mechanisms chosen and used to calculate regional stress are shown in Table 2 and Fig. 2b. Here we provide a brief description of the formal stress inversion method of Delvaux and Sperner, (2003), the “rotational optimization method”, that we performed in this study. The Win-Tensor program was used to perform the inversion scheme (available online at: http://www.damiendelvaux.be/Tensor/tensor-index.html).

The formal stress inversion of maximum shortening (P), maximum extension (T), and neutral axes (B) (the moment stress axes) are the source of the four parameters of the reduced stress tensor for the regional stress state.

The stress ratio (R) and the orientation of the three orthogonal principal stress axes (σ1, σ2, σ3, that is, σ1 ≥ σ2 ≥ σ3) is given by:

$$R = \sigma2 - \sigma3 / \sigma1 - \sigma3 \quad (3)$$

Formal stress inversion of the focal solutions should include two basic considerations (Mercier et al., 1991; Carey-Gailhardis and Vergely, 1992) as follows: uniform and invariant stress field in time and space, and the Wallace-Bott hypothesis, that the slip will have occurred in the direction of maximum shear stress (Bott, 1959).

The Rotational Optimization method seeks to minimize the misfit function for each event. The misfit function may be described using the misfit angle (α) and the fitness, which is the angle (α) between the estimated shear stress and the slip vector (Delvaux and Sperner, 2003). The nodal plane, which has the smaller misfit value, is assumed to represent the actual fault plane through comparing both nodal planes of each focal mechanism to a stress tensor. Thus, the focal planes best fitted to a uniform stress field are included in the final inversion procedure. Then, to estimate σ1, σ2, σ3 and R (Gephart and Forsyth, 1984), the fault planes selected are inverted. The fault slip and the initial tensor selected can also be used through the iterative grid search inversion scheme. This usage restricts and minimizes the target area during the inversion scheme (Delvaux and Barth, 2010) and also favors high shear stress and low normal stress on the plane to promote slip (Delvaux and Barth, 2010).

We also took into account "the tectonic stress regime index (R')", (Delvaux et al. 1997, 2007; Delvaux and Sperner, 2003) estimated to numerically define the stress regime using the simple relationship given as:

R' = R for normal faulting regimes (NF ranging between 0 to 1),
R' = (2 - R) for strike-slip regimes (SS ranging between 1 to 2),
R' = (2 + R) for thrust faulting regimes (TF ranging between 2 to 3). (4)

The resulting equal area projection images are shown in Figs. 8a and b. Fig. 8a shows NS and R (0.89) with σ1 (47/182), derived from regional CMT only, while Fig. 8b shows SS and R (0.83) with σ1 (00/344), derived from regional CMT plus GCMT. Both models indicate normal faulting with a strike-slip component (regional CMT only in Fig. 8a) and strike-slip

faulting (regional CMT plus GCMT in Fig. 8b) with a NNW-SSE striking maximum principal horizontal stress axis, parallel to the GPS slip vector in the region (Fig. 1a). Stability plots of σ1, σ2, σ3 and R' values, together with a Mohr circle diagram, obtained from regional CMT plus GCMT, are provided in S5 (Fig. S5), yielding the relatively low stress ratio R' = 1.17 ± 0.46 (R' = 2 - R).

4. Interpretation and discussion

4.1. Spatio-temporal distribution of aftershock focal mechanisms, Coulomb stress changes and co-seismic surface displacement

Distributional pattern of aftershock seismicity and focal mechanisms

In Fig. 2a, the ISC-located, compact aftershocks on and off both mainshocks can be observed at the NW and SE edges of both ruptures, respectively. The aftershocks are clustered in and around both mainshocks at depths ranging from 1-16 km, while a few tend to migrate and propagate semi-linearly from SE to NW. The depth of the SE-NW semi-linear aftershocks tends to smoothly increase to a maximum of 16 km, as the distance increases from the mainshocks (Fig. 2a). Fig. 2a also shows W-E and N-S vertical sections of the wedge-shaped aftershock cluster. The W-E profile shows a relatively narrow cluster at depths up to 16 km and that the activity NW of both mainshocks occurred between depths of 5 and 15 km. The N-S profile illustrates a relatively diffuse cluster and activity in the depth range 5-15 km in the mainshock area. Both profiles in Fig. 2b show the stepped-like, progradational aftershock pattern that progrades horizontally (through ~12 km to W and NW) and vertically (~5 to ~12 km), and almost symmetrical aftershock propagation that spreads bilaterally (through ~12 km to N and S) and vertically (~5 to ~12 km). The aftershock pattern gets progressively and gradually deeper toward the NW and the SW from ~5 to ~10 km depths, reaching the seismicity cut-off depth of around 12 km of the activity off the mainshocks. The located aftershocks (Fig. 2) show that the events ruptured the shallow upper crust towards the NW and SW (mainly in the depth range ~5-12 km).

In Fig. 2b, the focal mechanisms of the aftershocks show that, there were both strike-/oblique-slip events and almost pure normal-slip events along the co-seismic rupture, in addition to normal-slip focal mechanisms with little strike component. Much of the normal-slip focal

603 mechanisms, including K1 and the GCMT, have rake and dip angles between ~ -40° and ~ -
604 140° and ~30° and ~60°, respectively (Table 2). Most of events following both mainshocks
605 appear to show some degree of normal and strike-slip mechanisms, but largely exhibit strike-
606 /oblique-slip mechanisms (Fig. 2b), which are sequential and extend progressively and to
607 greater depths toward the NW. In Fig. 2b, these focal mechanisms and the NW-SE linearity of
608 the aftershocks indicate that the event activity was because of a right-lateral NW-SE oriented
609 fault located at the SE-end of the mainshock ruptures. The event activity gets shallower (~5-
610 10 km) in the SE where it first initiated and becomes gradually deeper, up to around 12 km, as
611 it extends towards the NW. In addition to the two right-lateral, pure strike-slip mechanism
612 aftershocks, two distinct focal mechanisms with reverse components are observed; one is pure
613 reverse-slip and one is reverse oblique-slip. These might be related to either the Coulomb
614 stress release or triggering (Fig. 3) due to co-seismic slips.
615
616 *Relation of focal mechanisms to co-seismic stress changes*
617
618 The spatio-temporal distribution of aftershocks from both the K1 and K2 events follows a
619 semi-linear, cluster-shaped pattern through a NW-SE strike direction of the mainshock
620 mechanisms (Fig. 2a) in a relatively narrow area, in which active extension and strike-slip
621 deformation co-occur (Fig. 2b) and where fault interaction was responsible for the spatio-
622 temporal clustering (Jordan et al., 2011). This suggests that stress changes on fault(s) caused
623 by K1 can be inferred from focal models of fault interaction(s) (Jordan et al., 2011).
624
625 During the time before both mainshocks, as shown Table 2 and Fig. 2b, pure strike-slip focal
626 mechanisms evolved and propagated through right-lateral strike-slip motion into pure normal-
627 slips that, in turn, propagated through normal slip motion, with the same and/or similar-size
628 magnitude of ~ 4.0 Mw at depths of 6-12 km (#1 to 4). When both mainshocks occurred (#5,
629 9), pure normal focal mechanisms (#8) evolved and propagated through right-lateral strike-
630 slip motion into normal-slip (#11) that propagated again through right-lateral strike-slip
631 motion and then to normal-slip (#17). The temporal evolution of these aftershock focal
632 mechanisms was completely loaded by co-seismic stress transfer (Figs. 3 and 6), suggesting a
633 cyclic motion of successively triggered aftershocks with repeated, normal-/strike-slips in the
634 depth range 6-11 km. During the period following both mainshocks, the continued cyclic
635 motion of normal- and strike-slip successive focal mechanisms was partly unloaded by

636 Coulomb stress transfer (Figs. 3 and 4). This suggests a relatively low seismicity of normal
637 oblique-slip motion in the depth range 6-10 km (#8, 9).
638
639 Thus, the faulting patterns of the aftershock focal mechanisms were closely controlled by both
640 extensional and right-lateral strike-/oblique-slip fault systems. They also appear to have an
641 episodic, repeated pattern of evolution, providing a comprehensible mechanism for the upper
642 crustal deformation.
643
644 *Relation of co-seismic stress changes to surface deformation*
645
646 Aftershock focal mechanisms showed that the strike direction of the normal focal mechanisms
647 changed first from NNW-SSE to N-S, then from N-S to NW-SE and subsequently to NNW-
648 SSE (nearly N-S) and eventually from N-S to NNE-SSW (#8, 11, Fig. 2b) during the whole
649 period of observations. These slight but progressive changes in the strike directions,
650 associated with the extension directions, resulted in a strike-slip transition of the faulting,
651 from normal (#5, 8) to right-lateral (#9), normal oblique-slip (#10), and transformed the upper
652 crustal deformation from an extension (#5) into a right-lateral transtension (#12 to 21). This
653 suggests upper crustal extension to a strike-slip transition along the SFZ and its transtensional
654 opening. In addition to transtensional deformation of the upper crust, the suggested spatio-
655 temporal evolution of the aftershock focal mechanisms indicates that K1 triggered K2 while
656 also activating multiple faults in the vicinity of the ruptures due to Coulomb stress transfer.
657 This indicates that the source fault rupture has not only loaded (Fig. 6), but also unloaded
658 surrounding receiver faults (Fig. 5). Cyclic fault loading and unloading implies that the
659 dynamic stress changes caused by propagating seismic waves interacting with the receiver
660 faults are spatio-temporally very complex (e.g., Fig. 4) (Jordan et al., 2011).
661
662 Multiple activation of the strike-/oblique-slip fault mechanisms, both off and on fault, shows
663 that they were initiated during K1 because of changes in co-seismic stress (Fig. 3 and Table
664 2). The spatial distribution of located aftershocks (Fig. 2b) indicates triggering of nearby
665 strike-slip and normal fault segments, situated in the areas where static stress has both
666 increased and decreased due to the K1 mainshock generation (Fig. 3). These areas are where
667 both positive and negative stress changes were co-located (Figs. 5 and 6). For example, in Fig.
668 6, a NW-SE trending stress triggering zone indicates an increase in shear stress and enhanced
669 seismicity at depths of 6-11 km, while a WNW-ESE or nearly W-E, stress shadow zone

indicates an increase in normal stress and reduced seismicity at 6-8 km deep (Fig. 5). The aftershocks triggered and activated by the enhanced seismicity with high shear stress indicate seismically highly active fault segments, while those deactivated by the reduced seismicity with high normal stress indicate aseismic release of shear stresses and suppressing earthquakes through the upper crustal depths, consistent with geodetic evidence of co-seismic subsidence through the stress shadow zone.

D-InSAR analysis of the co-seismic surface displacement (Fig. 7) revealed, as inferred from the interferogram image, that the K1 and K2 events caused surface deformations (Fig. 7a). As inferred from Fig. 7a, the conjugated, NW-striking and NE-striking multiple rupture propagation complex, are associated with the SFZ and BF, respectively. The NE-striking complex clearly follows through a zone of the NTS (Fig. 7b). The conjugate pattern of surface deformation indicates that the largest deformation gradients in the topography continued perpendicular to the NW and NE directions. This is the reason why the main deformation pattern increases from the SW to the NE. The direction of the largest deformation gradient is prominent towards the NE (Fig. 7a), in which the deformational feature of the NTS zone was evident (Figs. 7b, c). Moreover, as clearly shown in Figs. 7b and 7c, the surface is vertically fractured and displaced by a vertical rupture of ~20 cm (max) and ~5 cm (min) and asymmetrically downlifted (subsidence) by a distinct block rupture of between ~12 cm and ~15 cm, due to co-seismic surface deformation caused by both mainshocks, suggesting multiple deformation of the surface (Fig. 7a). In addition, the selection of the fault plane is well supported by strong evidence of vertical block displacement along the rupture and ~12 cm (min) of distinct subsidence towards the WSW or nearly W-E, consistent with evidence of the stress shadow zone (Figs. 4a, d and 5) through co-seismic subsidence (Figs. 7b, c). Correlative analysis of D-InSAR data supports the suggestion that the surface was multiply ruptured and/or multiply fractured as a result of the combined effects of the K1 and K2 events.

In summary, high shear stress triggering encompasses the behavior of earthquake-mediated fault interactions (Jordan et al., 2011) through focal mechanisms of aftershock clustering, suggesting Coulomb failure stress evolution of intraplate, pull-apart seismicity. Despite the uncertainty of the precise locations of events because of the absence of close field station data, such seismicity implies multi-segmentation along the SE-termination of the SFZ. As inferred from Figs. 7a and 7b, the seismicity appears to directly connect the SFZ to the BF

(Fig. 2a). We suggest that it is perhaps not surprising that, at some depths, the SFZ is connected directly to the BF (Fig. 2b). This is discussed further in the following subsection.

4.2. Pull-apart multiple activation of pre-existing faults through strain partition

Results obtained from seismological and geodetic analyses show that the consecutive K1 and K2 mainshocks and the associated aftershock sequences may have been involved in the co-seismic activation of the SE-segments of the SFZ and the predominance of right-lateral strike-/oblique-slip motions, partially in keeping with the results of Taymaz et al., (2022). In the other hand, the results inverted from stress tensors (regional CMT plus GCMT data in Fig. 8b) reveal a main stress pattern and a present-day "extensional strike-slip tectonic stress regime" derived from inversion of focal data as described earlier, where the strike-slip movement on the faults has a right-lateral movement (e.g., Fig. 1a). The main stress pattern is closely compatible with the angle range ~45º-50º between the slip vector of GPS, parallel to NNW-SSE, and the NW-SE striking faults in the region (see Fig. 1a). This may provide useful insights into the sources of seismicity, the conditions for slip and the weaknesses of pre-existing structural lineaments.

The co-seismic activation of the fault segments may be interpreted as reactivation of pre-existing faults (Sibson 1989; Raleigh et al., 1972; Zoback, 1992), rather than the development of new faults, given that the angle between the fault and principal stress direction in slip vector plane was between ~25º and ~55º (Raleigh et al., 1972; Zoback, 1992). This generally corresponds to the angular difference between strike and maximum principal stress azimuth in strike-slip faulting of between ~20º and ~60º, with dips between ~40º and ~80º. This arrangement of the fault planes is consistent with slip in pre-existing faults, rather than formation of new faults (Zoback, 1992) and is also compatible with the regional stress field (Fig. 8b). This suggests the reactivation of pre-existing faults in an uniformally oriented regional stress field (Zoback, 1992).

The consistency of all focal solutions (Fig. 2b) with co-seismic surface deformation (Fig. 7) and Coulomb stress changes (Figs. 3-6) is a strong constraint on the main stress state, suggesting extensional and strike-slip stress arrangements of the compressional tectonic regime (Fig. 8b) as discussed elsewhere (Toker and Pınar, 2024). Furthermore, strike-slip and normal fault planes are the two main fault sets triggered and reactivated during both the K1

738 and K2 events. This implies that both fault systems have a similar role when accommodating
739 active deformation. For example, the dipping of the fault planes (e.g., ~30º in Table 2) could
740 indicate flattening of the affected fault segment at centroid depths of ~12-15 km as an
741 optimally oriented, structural discontinuity "detachment" inside the fault zone with finite
742 width. Thus, the coexistence of extensional and strike-slip faults within a given block wedge
743 (Fig. 2) can be interpreted in two ways. The first is a simple extruding wedge block, in which
744 a single state of stress prevails (e.g. Cisternas and Philip 1997). The second interpretation
745 would be a partitioning of slip on normal and strike-slip faults (e.g. Jackson 1992), in
746 accordance with the mean regional stress state (Fig. 8b).
747
748 Indeed, in Figs. 7b and 7c, the geodetic data associated with the segments of seismicity offset
749 and available focal mechanisms indicate a highly extended and asymmetrically subsided
750 basin. This implication would correlate well with a relatively large, pull-apart wedge block,
751 which was strongly tilted due to high normal stress, through a nearly W-E trending stress
752 shadow zone towards the W, where the seismicity was limited and/or reduced by suppressing
753 earthquakes (e.g., Fig. 5). Thus, the pull-apart motion of the wedge block appears as an
754 aseismic crustal feature associated with an immature SFZ. However, due to sparse coverage
755 of the station network and lack of near-field data, it is not clear if the segmentation of the SFZ
756 observed at the surface, responsible for the pull-apart block motion where K1 and K2
757 occurred, is supported at crustal depths by a simple and/or complex pattern of
758 microearthquakes associated with the SFZ and/or BF (Fig. 2a).
759
760 A pull-apart tectonic mechanism derived from our combined data sets favors the westward
761 transfer of upper crustal material as an obliquely extruding wedge block. This would account
762 for the pull-apart fragmentation and separation, with partitioning of deformation on spatially
763 separated sub-parallel/parallel normal faults and strike-slip faults (e.g. Jackson 1992), in
764 accordance with the NNW direction of mean regional compression (e.g., Toker and Pınar,
765 2024). In the context of intraplate seismicity, these faults may have been selectively
766 reactivated by local variations in pore pressure, fault friction, and/or strain positioning
767 (Zoback, 1992) in favorably oriented lower crustal ductile shear zones, formed during earlier
768 episodes of crustal deformation (Zoback et al., 1985; Zoback, 1992). The presence of the pull-
769 apart systems along and across the Arabia-Eurasia convergence zone, including the high
770 collisional plateaus of E-Anatolia and NW-Iran, is not a novel proposition. On the contrary,
771 the pull-apart deformation and basin formation associated with multiple segmentation of

faults observed along the MRF across the Zagros collision zone and also along the NTF in NW Iran have been extensively reported (Tchalenko and Braud, 1974; Talebian and Jackson, 2002; Copley and Jackson, 2006; Authemayou et al., 2009; Atmaoui and Kukowski, 2006; Peyret et al., 2008; Sepahvand et al., 2012; Moradi et al., 2011; Soleymani Azad et al., 2015, 2019; Aflaki et al., 2021; Niassarifard et al., 2021).

The following subsection further examines the most plausible model of fault reactivation and block extrusion and discusses their physical basis, using concepts of intraplate seismicity, and our new and previous data sets (geodetic strain-rate field from Toker and Pınar, 2024). The following inferences are not only unique, but they are also the simplest way to explain our observations.

4.3. Physical understanding of SFZ and BF activation and oblique block extrusion on suture zone

An important role of pull-apart, multiple activation in an intraplate crustal stress field is that low-level, permanent deformation of the crust occurring along pre-existing zones of weakness, for example suture zones (e.g., Toker and Pınar, 2024), results in reactivation of major faults or basement structures. Thus fault reactivation would happen when the resolved shear stress in the fault plane exceeded the shear resistance to movement, as has been suggested by many authors previously (Donath and Cranwell, 1981; Etheridge, 1986; Sibson, 1985; White et al., 1986; and Etheridge et al., 1991).

Upper crustal reactivation of low-strength pre-existing SFZ and BF

As recognized in the tectonic sketch map (Fig. 9a) interpreted from a combined data set of available geophysical and geological studies, the linked normal fault/strike-slip fault/detachment system characteristic of extensional orogeny (Etheridge et al., 1991) provides a better explanation for both extensional reactivation of the "NTS" zone between E-Anatolia and NW-Iran (NTS in Figs. 1a, 7b, c, and 9a), and also the upper crustal material wedged by the strike-slip SFZ and BF. This typifies the reactivation of extensional basin-forming structures, as proposed by Etheridge in 1986 under various styles of stress orientations (Etheridge, 1986; Etheridge et al., 1991). Indeed, in this case it is one that involves stresses oblique to the pre-existing structures, giving rise to strike- and/or oblique-

slip reactivation of the SFZ and BF (Etheridge et al., 1991). This indicates that the strike-slip faults, SFZ and BF, and related small-scale, discontinuous structures develop above strike-slip reactivated normal faults or *vice versa* (Etheridge et al., 1991). During strike-slip and/or extensional reactivation of the SFZ and BF the transfer offsets act as releasing bend(s), localizing discrete pull-apart multiple structure(s) in a crustal stress field. This is also consistent with the regional stress model, proposed by Iio and Kobayashi, (2002), which may explain the occurrence of intraplate the K1 and K2 earthquakes on "low-strength pre-existing faults" in the upper crust (Sykes, 1978; Hinze et al., 1988; Johnston and Kanter, 1990; Zoback, 1992; Iio and Kobayashi, 2002) and in the specific areas of the NTS zone closer to SE- and NE-terminations of the SFZ and BF, respectively (Fig. 9a). Thus, stresses, due either to increased temperatures or high water content (Goetze and Evans, 1979; Griggs and Blacic, 1965) accumulate by successive K1- and K2-like earthquakes and their aftershocks in areas adjacent to segments of the SFZ and BF, and thus through the upper crust above regions of low viscosity in the lower crust and/or upper mantle (the low-strength model by Liu and Zoback, 1997; Kenner and Segall, 2000; Iio and Kobayashi, 2002).

Therefore, the hypothesis to be tested is that the K1 and K2 events resulted in extensional fragmentation of the NTS zone (Figs. 7b, c) and, thus, separation of the E-Anatolia block from the NW-Iranian block (Fig. 9a) all along the roughly N-S striking curvilinear NTS zone (Fig. 1a). This hypothesis is supported by the seismicity, tectonics and GPS studies of Solaymani Azad et al., (2015, 2019), Niassarifard et al., (2021) and Toker and Pınar, (2024). For example and as shown in Fig. 9a, the NE-SW continuation of the BF is distinctly subparallel to the NTS zone, and its SW-termination is morphologically characterized by only around 10 km (max) of lateral separation from the NTS zone and a peculiar "volcano-magmatic" depression (Yesilova et al., 2021; Yesilova, 2021, 2022). The separation is also suggested by W-E extensional fracturing of an individual volcanic dome, located in an area of NW-Iran, similar to the extensional Mount Ararat (Ağrı) in the furthest N of the NTS (Fig. 1a) (see Solaymani Azad et al., 2015). Further evidence of extensional and transtensional deformation of the NTS is provided in section S6 (Fig. S6); NNW- and SSE-terminations of the NTS are shown in Figs. S6a and S6b, respectively (see Toker and Pınar, 2024 for geodetic strain-rate field data and fault focal mechanisms).

Aseismic block extrusion

The most important point concerning these inferences is the suggestion of aseismic extrusion of the upper crustal block, accommodated by the SFZ and BF (Fig. 9a) above low viscosity region(s), possibly confined to a localized ductile fault zone (Iio, 1996; Stuart et al., 1997), or widely distributed in a volume (Liu and Zoback, 1997; Kenner and Segall, 2000; Iio and Kobayashi, 2002). Evidence comes from a wide range of data sets of earlier geophysical studies in the area. A projected N-S trending cross-sectional profile (A-B axis, Fig. 9a) reveals spatial variations of estimated Gravity/Bougger anomalies from surface to asthenosphere (data cross-section from Mahatsente et al., 2018) (Fig. 9b). Joint tectonic interpretation, combined with crustal geophysical data compiled from Mahatsente et al., (2018) and Artemieva and Shulgin (2019), proposes heat-weakened, low density crust, extensive thermal heterogeneity and distinct crustal segmentation in the study area (Fig. 9b). In Fig. 9b, a low heat flow-low Bougger anomaly and high Moho temperature-high crustal velocity, together with high sediment thickness (data compiled from Artemieva and Shulgin, 2019) do indeed indicate thermally weakened, highly ductile, and asymmetrically subsiding crust that explains the low-strength regional stress model (e.g., Toker and Pınar, 2024). This model can explain the consecutive occurrence of upper crustal K1 and K2 events above the low viscous-low density areas, widely distributed in a crustal volume (Fig. 9b) (Liu and Zoback, 1997; Kenner and Segall, 2000; Iio and Kobayashi, 2002).

In the case of conjugate SFZ and BF, as shown in Fig. 9a, it is clear that lateral displacement along the BF and small-scale strike-slip segments of the SFZ accommodate northward collision in the study area. In map view, shown by Fig. 9a, strike-slip features of the BF and SFZ trend primarily NE-SW and NW-SE, forming a crustal block in the form of a rhombic hexahedron, which exhibits lateral extrusion accommodated by the SFZ and BF. Left- and right-lateral shearing along the BF and SFZ, respectively, thus guide the local crustal block laterally, away from the collision. In tectonic extrusion of a rhombohedron-block (Tapponnier et al., 1986), a discrete portion of crust moves away from the point as a whole but undergoes internal deformation with much bulk strain at the edges of the planes. The small-scale, discontinuous right-lateral strike-slip segmentation of the SFZ and the simple left-lateral feature of the BF clearly exhibit these traits, while accommodating the far-field effects of N-S shortening/E-W extension. This, in turn, allows small-scale aseismic deformation and local block rotation, converting shear stress into extensional deformation expressed as releasing bends and strong subsidence (Fig. 9a). As a result, the SFZ and BF facilitate the transfer of an upper crustal extrusion block to the WNW. This mechanism explains the extensional

874 fragmentation and separation with partitioning of deformation all along the zone of the NTS,
875 in agreement with the NNW direction of mean regional compression. This provides a valuable
876 geodynamic insight into a possible occurrence of extensional orogeny (Collins, 2002) in and
877 along the further E-termination of the E-Anatolian block (Toker and Pınar, 2024), which may
878 be assumed to be the ECWIB, as interpreted by Rolland, (2017).
879
880 **4.4. Geodynamic aspects of extension and strike-slip division of convergence**
881
882 The E-termination of the E-Anatolian block is characterized by a curvilinear zone of the NTS
883 (Fig. 1a) (Toker and Pınar, 2024), within which the SFZ and BF accommodate the
884 convergence (Fig. 9a) with the strain being separated into extensional and strike-slip
885 components ("strain partitioning" in Allen et al., 2011; Copley and Jackson, 2006; Jackson,
886 1992; Toker and Pınar, 2024; Niassarifard et al., 2021). In Fig. 1a, the NW–SE trending right-
887 lateral strike-slip faults along the NTS also contribute to general regional convergence
888 through this division of strain, very similar to the SFZ (Fig. 9a). Given that the main faulting
889 along the NTS predominantly trends NW–SE, as a combination of thrust/normal faults and
890 strike-slip shear zones (e.g. Sarkarinejad et al. 2008), the occurrence of strain partitioning
891 seems likely in the NTS (Allen et al., 2011) and may also explain the NE–SW left-lateral BF
892 (Fig. 9a). Strain partitioning is typically one of the main seismotectonic characteristics of E-
893 Anatolia and NW-Iran, as discussed elsewhere (Niassarifard et al., 2021; Toker and Pınar,
894 2024) and below.
895
896 An evidence for oblique normal faulting, as reported by Copley and Jackson, (2006), between
897 NW-Iran and E-Turkey (Fig. 1a), the strain has apparently been partitioned into pure normal
898 faulting and strike-slip faulting (Copley and Jackson, 2006) in the Serow normal faults (SF),
899 with a slip vector of 250° to 260° (i.e., the overall slip vector near this fault plane, 290° to
900 300°) (Copley and Jackson, 2006). As an example, the Salmas earthquake of 1930, with
901 surface rupture striking NW-SE, involved equal elements of normal slip and right-lateral slip
902 (Tchalenko and Berberian, 1974; Berberian and Tchalenko, 1976; Copley and Jackson, 2006),
903 indicating a slip vector similar to that estimated for the other normal faults reported by Copley
904 and Jackson, (2006). In NW Zagros, for example, strain partitioning is exhibited by NE-SW
905 shortening along the SW front of the Zagros and NW-SE right-lateral strike slip on the MRF
906 to the NE (Talebian and Jackson, 2004; Copley and Jackson, 2006) (Fig. 1a). A few right
907 lateral faults cutting through the central section of the Zagros strike roughly N-S, allowing for

accommodation of along-strike extension in the Zagros (Talebian and Jackson, 2004) and also connect the region with strain partitioning in the NW to the zone of orthogonal convergence in the E (Blanc et al., 2003; Allen et al., 2006). Another distinct example is observed in the TIHP (Fig. 1a). Interestingly, there does not appear to be any seismic evidence for active shortening on the S-margin of the E-Anatolia-NW-Iranian region itself, except for the Greater Caucasus which acts as the region of shortening to the NW of the Zagros (Copley and Jackson, 2006). Furthermore, the NW-SE-trending right lateral MRF bounds the NE-margin of the Zagros, indicating spatial separation of the convergence into strike-slip and dip-slip components (Copley and Jackson, 2006). The MRF ends in the NW (~36.7ºN, ~45.1ºE), where investigation of seismicity suggests that the S-margin shortening of the collision zone is almost absent (Copley and Jackson, 2006). Moreover, the two pull-apart basins are prominent near the NW-end of the MRF (Copley and Jackson, 2006) (Fig. 1a). In 1970, an earthquake occurred near these two basins. The focal mechanism was shown to be oblique right-lateral and normal motion, with a slip vector of ~280º to ~290º (Copley and Jackson, 2006).

The slip vector for the MRF at about 34ºN is ~300º to ~310º (Talebian and Jackson, 2002; Copley and Jackson, 2006), while the SF also has a similar slip vector of ~290º to ~300º (Copley and Jackson, 2006), but there is no known continuous fault forming a link between the MRF and the SF (Copley and Jackson, 2006) (Fig. 1a). However, it has been suggested that the motion of the normal faults was because of continuation of movement of the MRF to the NW ‘‘linking’’ the MRF with right-lateral strike-slip faults near Lake Van and explaining the existence of the normal faults (Copley and Jackson, 2006). This means that the NW continuation of the MRF to ~38.5ºN, ~44.0ºE (Fig. 1a) links the MRF directly with right-lateral strike-slip faults, including the SFZ, DF, and HTGF (see Fig. 9a, E-part of the Lake Van area). This would explain the occurrence of pull-apart seismicity within a zone of the NTS. This explanation is consistent with the present arrangement of a series of right-lateral faults through NTS that strike N-S in a curvilinear fashion, and also with a band of oblique normal faults running NNW-SSE along the Turkey-Iran border (Fig. 1a), as discussed elsewhere (Allen et al., 2004, 2006; Copley and Jackson, 2006; Solaymani Azad et al., 2015, 2019; Niassarifard et al., 2021; Toker and Pınar, 2024). Previous tectonic studies explained this previously unrecognized extensional/transtensional deformational regime by rapid changes in direction and speed of movement of the Arabia-Eurasia convergence close to the Euler pole, and to the NW termination of the MRF (Copley and Jackson, 2006). Such a

942 radical change in the nature of the faulting within the collision zone has been interpreted as
943 occurring because of a doming hot asthenosphere and large plateau uplift, due to slab
944 delamination and break off process, as discussed elsewhere (Angus et al., 2006; Bartol and
945 Govers, 2014, Delph et al., 2015; Mahatsente et al., 2018; Reid et al., 2019; Artemieva and
946 Shulgin, 2019; Toker and Şahin, 2019, 2022; Toker and Pınar, 2024 and references therein)
947 and migration of deformation to the edges (Allen et al., 2004; Copley and Jackson, 2006;
948 Toker and Pınar, 2024). This would modify the upper mantle temperature distribution (Bartol
949 and Govers, 2014; Mahatsente et al., 2018; Artemieva and Shulgin, 2019; Toker and Şahin,
950 2019, 2022 and references therein) and lead to widespread asthenospheric underplating
951 (Mahatsente et al., 2018, Toker and Şahin, 2019) some time between the onset of continental
952 shortening at ~12 Ma (Dewey et al., 1986; McQuarrie et al., 2003), and the recognized change
953 in the nature of the collision zone at ~ 5 Ma (Copley and Jackson, 2006).
954
955 Finally, the conjugate faults, the SFZ and BF, appear to simply transport a wedge-shaped
956 piece of detached upper crust laterally away from a zone of the N-S collision (Fig. 9a). Both
957 faults achieve the shortening, not only by partitioning of oblique convergence, but also
958 through vertical rotation about their axes. Such an accommodation of the shortening may have
959 been due to the orientation of inherited structures and crustal weakness, as proposed by Allen
960 et al., (2006), together with segmentation and differentiation of thermally weakened crust
961 (Mahatsente et al., 2018, Toker and Şahin, 2022) because of mechanical and thermal
962 alterations of the lithosphere beneath E-Anatolia (Artemieva and Shulgin, 2019; Reid et al.,
963 2019). The thermal weakening effect of the appearance of warmer mantle material creates
964 asthenospheric flow transport inside E-Anatolia and the NTS (Toker and Pınar, 2024). The
965 NTS is thus infused and shaped by the flow of mantle. This triggers and drives lateral
966 movement of convergent crustal blocks. The convergence mechanism is dominated by strain
967 partition deformation, resulting from slab thinning or absence. As detailed in Fig. 9a, such
968 weakness is indicated in Fig. 7 and may be interpreted as a zone of the NTS that approximates
969 to the fragmentary border between the E-Anatolian and NW-Iranian blocks (Toker and Pınar,
970 2024). A similar explanation has been proposed for the MRF of the Zagros, which also
971 approximately follows the old Arabia-Eurasia suture (Allen et al., 2006).
972
973
974
975

5. Implications and conclusions

The integrated seismological, geodetic, and stress-field analyses consistently show that the 23 February 2020 Khoy–Qotour earthquake sequence was controlled by mechanically coupled but kinematically distinct fault systems within the NTS zone. The Mw 5.6 mainshock ruptured a nearly N–S-striking normal fault, whereas the Mw 5.8 mainshock ruptured a NW–SE-striking right-lateral strike-slip fault at shallow depth (~8 km). Together with the relocated aftershock sequence, these results demonstrate that deformation was concentrated within an upper-crustal domain where extension and strike-slip faulting coexist and evolve through strain partitioning.

Coulomb stress modelling indicates that the first mainshock promoted failure on neighbouring normal and strike-slip faults, producing a NW–SE-trending zone of stress increase associated with enhanced seismicity and a W–E-oriented stress-shadow zone characterized by aseismic stress release. The spatial correspondence between stress transfer, focal mechanisms, and D-InSAR deformation confirms that rupture propagation was governed by stress interaction among pre-existing fault segments rather than by the reactivation of a single continuous fault.

Stress tensor inversion defines an extensional strike-slip regime under NNW–SSE maximum horizontal compression, in agreement with focal mechanisms, Coulomb stress changes, geodetic observations, and regional GPS-derived deformation. This consistency demonstrates that the earthquake sequence accommodated oblique Arabia–Eurasia convergence through coupled normal and strike-slip faulting, rather than by simple strike-slip deformation alone.

The combined observations support a pull-apart tectonic model in which deformation is partitioned between spatially separated but mechanically linked fault systems. Oblique upper-crustal extrusion toward the WNW, together with aseismic transfer of crustal material across the pull-apart domain, provides a coherent explanation for the observed deformation pattern and the evolution of the earthquake sequence.

More broadly, our results suggest that inherited structures within the NTS zone play a fundamental role in localizing transtensional deformation during continental collision. We propose that the Khoy–Qotour earthquake sequence represents ongoing fragmentation of the suture and progressive kinematic separation between the E-Anatolian and NW-Iranian blocks.

This mechanism provides a new framework for understanding strain partitioning, crustal extrusion, and earthquake generation within the Arabia–Eurasia collision zone and may be applicable to other inherited suture systems undergoing oblique convergence.

Acknowledgements

The authors would like to thank the Earthquake Department of the Disaster and Emergency Management Presidency (AFAD, Turkey), the Kandilli Observatory and Earthquake Research Institute (KOERI, Turkey), the International Seismological Center (ISC) and the Incorporated Research Institutions for Seismology (IRIS) Data Management Center for sharing earthquake data. The figures are plotted using Generic Mapping Tools (GMT) (Wessel and Smith, 1998). The shaded relief topography from global multiresolution terrain elevation data (USGS/NASA SRTM15+) has been provided by CIAT-CSI (http://srtm.csi.cgiar.org). This work is partly supported by a research fund of AFAD (Grant Number: AFAD-UDAP-G-20-07 by Irmak et al., 2022, and thanks to Dr. T. Serkan Irmak) and fully supported by a research fund of the Yuzuncu Yıl University (under Scientific Research Project Grant Number: FBA-2022-9799). D-InSAR data processing and related image analyses have been performed by Dr. Aydın Üstün (thanks to Dr. Aydın Üstün). The authors are extremely thankful to the Editor-in-Chief and the two anonymous reviewers for their critical comments and suggestions, which helped us to improve the current manuscript considerably.

References

AFAD, 2020, 23 Şubat 2020 Khoy (İran) Mw 5.9 Depremlerine İlişkin Ön Değerlendirme Raporu, Afet ve Acil Durum Yönetimi Başkanlığı (in Turkish).

Aflaki, M., Shabanian, E., Sahami, S., Arshadi, M., 2021, Evolution of the stress field at the junction of Talesh-Alborz-Central Iran during the past 5 Ma: implications for the tectonics of NW Iran, Tectonophysics, 821, 229115, https://doi.org/10.1016/j.tecto.2021.229115.

Allen, M., Blanc, B., Walker, R., Jackson, J., Talebian, M., Ghassemi, M. R., 2006, Contrasting styles of convergence in the Arabia-Eurasia collision: Why escape tectonics does not occur in Iran, Geol. Soc. Amer. Spec. Paper, vol. 409, pp. 579–589.

Allen, M., Jackson, J., Walker, R., 2004. Late Cenozoic reorganization of the Arabia-Eurasia collision and the comparison of short-term and long-term deformation rates. Tectonics 23, TC2008. http://dx.doi.org/10.1029/2003TC001530.

Allen, M.B., Kheirkhah, M., Emami, M.H., Jones, S.J., 2011. Right-lateral shear across Iran and kinematic change in the Arabia-Eurasia collision zone. Geophysical J. International 184, 555-574.

Ambraseys, N., Melville, C.P., 1982. A history of Persian earthquakes. Cambridge Earth Science Series. Cambridge University Press, London.

Angus, D.A., Wilson, D.C., Sandvol, E., and Ni, J.F., 2006, Lithospheric structure of the Arabian and Eurasian collision zone in eastern Turkey from *S*-wave receiver functions: Geophysical Journal International, v. 166, p. 1335-1346, doi: 10.1111/j.1365-246X.2006.03070.x.

Artemieva, I., Shulgin, A., 2019. Geodynamics of Anatolia: lithosphere thermal structure and thickness. Tectonics 38, 1–23. https://doi.org/10.1029/2019TC005594.

Atmaoui N, Kukowski N (2006) Initiation and development of pull-apart basins with Riedel shear mechanism: insights from scaled clay experiments. Int J Earth Sci 95: 225–238.

Authemayou C, Bellier O, Chardon D, Benedetti L, Malekzade L, Claude C, Angeletti B, Shabanian E, Abbassi M.R., (2009) Quaternary slip–rates of the Kazerun and the Main Recent

1065 Faults: active strike–slip partitioning in the Zagros fold–and–thrust belt. Geophys J Int 178:
1066 524–540. doi:10.1111/j.1365-246X.2009.04191.x

1067 Bartol J. and R. Govers (2014), A single cause for uplift of the Central and Eastern Anatolian
1068 plateau? Tectonophysics 637, 116–136.

1069 Berberian, M., 1976, on the evidence of the youngest activity of the North Tabriz fault and the
1070 seismicity of Tabriz city, Geol. Surv. Iran Rep., vol. 39, pp. 397–418.

1071 Berberian, M., 1981. Active faulting and tectonics of Iran. In: Gupta, H.K., Delaney, F.M.
1072 (Eds.), Zagros–Hindu Kush–Himalaya Geodynamic Evolution. American Geographical
1073 Union, Washington, DC, pp. 33–69.

1074 Berberian, M., 1994. Natural hazards and the first earthquake catalog of Iran. Historical
1075 Hazards in Iran Prior 1900, I.I.E.E.S. Report. vol. 1.

1076 Berberian, M., 1995. Master "blind" thrust faults hidden under the Zagros folds: active
1077 basement tectonics and surface morphotectonics. Tectonophysics 241, 193–224.

1078 Berberian, M., 1997, Seismic sources of the Transcaucasian historical earthquakes in
1079 Historical and Prehistorical Earthquakes in the Caucasus, D. Giardini and S. Balassanian, Eds.
1080 Dordrecht, The Netherlands: Kluwer, pp. 233–311.

1081 Berberian, M., 2014, Earthquakes and Co-seismic Surface Faulting on the Iranian Plateau: A
1082 Historical, Social, and Physical Approach. Developments in Earth Surface Processes 17, 776
1083 pp. Elsevier Book Series. ISBN:978–0–444-63,292-0.
1084 In:https://www.sciencedirect.com/bookseries/developments-in-earth-surface-
1085 processes/vol/17/suppl/C.

1086 Berberian, M., and J. S. Tchalenko, 1976, Field study and documentation of the 1930 Salmas
1087 (Shahpur-Azarbaidjan) earthquake, in Contribution to the Seismotectonics of Iran, part II,
1088 edited by M. Berberian, Rep. 39, pp. 271 – 342, Geol. Surv. of Iran, Tehran.

1089 Berberian, M., Arshadi, S., 1976. On the evidence of the youngest activity of the North Tabriz
1090 fault and the seismicity of Tabriz city. Geol. Surv. Iran Rep. 39, 397–418.

1091 Berberian, M., Yeats, R.S., 1999. Patterns of historical earthquake rupture in the Iranian
1092 plateau. Bull. Seismol. Soc. Am. 89, 120–139.

1093 Bertero, V., Frohmberg, K., Gath, E., Greene, M., Hays, W., Power, M., Youd, T.L., 1994.
1094 Liquefaction, Earthquake Basics Brief No.1 Free publication of Earthquake Engineering
1095 Research Institute (EERI), USA (8P).

1096 Blanc, E.J.-P., Allen, M.B., Inger, S., and Hassani, H., 2003, Structural styles in the Zagros
1097 Simple Folded Zone, Iran: Journal of the Geological Society of London, v. 160, p. 400–412.

1098 Bondár, I. and D.A. Storchak (2011). Improved location procedures at the International
1099 Seismological Centre, Geophys. J. Int., 186, 1220-1244, doi: 10.1111/j.1365-
1100 246X.2011.05107.x

1101 Bott, M.H.P., 1959. The mechanisms of oblique slip faulting. Geol. Mag. 96, 109-117.

1102 Bouchon, M., 1981. A simple method to calculate Green's functions for elastic layered media.
1103 Bulletin of the Seismological Society of America, 71(4), pp.959-971.

1104 Carey-Gailhardis, E., Vergely, P., 1992. Graphical analysis of fault kinematics and focal
1105 mechanisms of earthquakes in term of stress; the right dihedra method, use and pitfalls. Ann.
1106 Tect VI (1), 3-9.

1107 Chen, C. and H. A. Zebker (2000). “Network approaches to two-dimensional phase
1108 unwrapping: intractability and two new algorithms”. In: Journal of the Optical Society of
1109 America A 17, pp. 401–414.

1110 Chen, K. H., R. Bürgmann, and R. M. Nadeau (2010). Triggering effect of M 4-5 earthquakes
1111 on the earthquake cycle of repeating events at Parkfield, California, B. Seismol. Soc. Am.,
1112 100, 522-531.

1113 Cisternas, A., Philip, H., 1997. Seismotectonics of the Mediterranean region and the
1114 Caucasus. In: Giardini, D., Balassanian, S. (Eds.), Historical and prehistorical earthquakes in
1115 the Caucasus. Kluwer Academic Publishing, Dordrecht, Netherlands, pp. 39–77.

1116 Cocco, M., and J. R. Rice (2002). Pore pressure and poroelasticity effects in Coulomb stress
1117 analysis of earthquake interactions, J. Geophys. Res., 107, ESE 2-1 to 2-17,
1118 doi:10.1029/2000JB000138.

1119 Collins, W.J., 2002, Nature of extensional accretionary orogens, Tectonics, v. 21, no. 4, 1024,
1120 10.1029/2000TC001272.

1121 Copley, A., Faridi, M., Ghorashi, M., Hollingworth, J., Hackson, J., Nazari, H., Oveisi, B.,
1122 Talebian, M., 2013. The 2012 August 11 Ahar earthquakes: consequences for tectonics and
1123 earthquake hazard in the Turkish–Iranian Plateau, Geophys. J. Int., doi:10.1093/gji/ggt379.

1124 Copley, A., Jackson, J., 2006. Active tectonics of the Turkish–Iranian Plateau. Tectonics 25,
1125 TC6006. http://dx.doi.org/10.1029/2005TC001906.

1126 Delph, J.R., Zandt, G., Beck, S.L., 2015, A new approach to obtaining a 3D shear wave
1127 velocity model of the crust and upper mantle: An application to eastern Turkey,
1128 Tectonophysics, http://dx.doi.org/10.1016/j.tecto.2015.09.031.

1129 Delvaux, D., Barth, B., 2010. African stress pattern from formal inversion of focal mechanism
1130 data. Tectonophysics 482, 105-128.

1131 Delvaux, D., Macheyeki, A.S., Kervyn, F., Petermans, T., Verbeeck, K., Temu, E. B., 2007.
1132 Session TS3.3/NH4.4. Earthquake Geology of the Kanda Fault System (Tanganyikaerukwa
1133 Rift, SW Highlands of Tanzania). EGU General Assembly 2007, vol. 9. Earthquake Geology.
1134 Geophys. Res. Abstr, Vienna, p. 09129.

1135 Delvaux, D., Moeys, R., Stapel, G., Petit, C., Levi, K., Miroshnichenko, A., Ruzhich, V.,
1136 Sankov, V., 1997. Paleostress reconstructions and geodynamics of the Baikal region, Central
1137 Asia. Part II: Cenozoic rifting. In: Cloetingh, S., Fernandez, M., Munoz, J.A., Sassi, W.,
1138 Horvath, F. (Eds.), Structural Controls on Sedimentary Basin Formation: Tectonophysics,
1139 282, pp. 1-38.

1140 Delvaux, D., Sperner, B., 2003. Stress tensor inversion from fault kinematic indicators and
1141 focal mechanism data: the TENSOR program. In: Nieuwland, D. (Ed.), New Insights into
1142 Structural Interpretation and Modelling, vol. 212. Geol. Soc. Lond. Spec. Publ., pp. 75-100.

1143 Dewey, J.F., Hempton, M.R., Kidd, W.S.F., Saroglu, F., Sengor, A.M.C., 1986. Shortening of
1144 continental lithosphere: the neotectonics of eastern Anatolia, a young collision zone. Geol.
1145 Soc. Spec. Publ. 19, 3-36.

1146 Dhont, D., and Chorowicz, J., 2006. Review of the neotectonics of the Eastern Turkish–
1147 Armenian Plateau by geomorphic analysis of digital elevation model imagery. Int., J Earth
1148 Sci., Geol Rundsch, 95: 34–49 doi 10.1007/s00531-005-0020-3.

1149 Djamour, Y., Vernant, P., Nankoli, H. R., Tavakoli, F., 2011. NW Iran-eastern Turkey
1150 present-day kinematics: results from the Iranian permanent GPS network. Earth Planet S. C.
1151 Lett. 307 (1-2), 27-34.

1152 Donath, F., and Cranwell, R. M., 1981. Probabilistic treatment of faulting in geologic media.
1153 In: Mechanical behaviour of crustal rocks, N. L. Carter, M. Friedman, J. M. Logan, and D.W.
1154 Stearns (Eds.). American Geophysical Union Monograph 24, 231-241.

1155 Etheridge, M., 1986. On the reactivation of extensional fault systems. Phil. Trans. Roy. Soc.
1156 Lond., A 317, 179-194.

1157 Etheridge, M., McQueen, H., and Lambeck, K., 1991. The Role of Intraplate Stress in
1158 Tertiary (and Mesozoic) Deformation of the Australian Continent and its Margins: A Key
1159 Factor in Petroleum Trap Formation, Exploration Geophysics 22: 123-128.

1160 Farr, T.G. et al. (2004). "The Shuttle Radar Topography Mission". In: Rev. Geophys. 17.
1161 doi:10.1029/2005RG000183.

1162 Fojtíková, L., Vavryčuk, V., Cipciar, A. and Madarás, J., 2010. Focal mechanisms of micro-
1163 earthquakes in the Dobrá Voda seismoactive area in the Malé Karpaty Mts. (Little
1164 Carpathians), Slovakia. Tectonophysics, 492(1-4), pp.213-229.

1165 Fréchet, J., 1985. Sismogenèse et doublets sismiques. Thèse d'État, Université Scientifique et
1166 Médicale de Grenoble, 206 pp.

1167 Gephart, J.W., Forsyth, D.W., 1984. An improved method for determining the regional stress
1168 tensor using earthquake focal mechanism data: application to the San Fernando earthquake
1169 sequence. J. Geophys. Res. 89 (B11), 9305-9320.

1170 Ghods, A., Shabanian, E., Bergman, E., Faridi, M., Donner, S., Mortezanejad, G., and Aziz-
1171 Zanjani, A., 2015, the Varzaghan-Ahar, Iran, Earthquake Doublet (Mw 6.4, 6.2): implications
1172 for the geodynamics of NW-Iran, Geophys. J. Int. 203: 522-540. doi: 10.1093/gji/ggv306.

1173 Goetze, C. and B. Evans, 1979, Stress and temperature in the bending lithosphere as
1174 constrained by experimental rock mechanics, Geophys. J. R. Astron. Soc., 59, 463–478.

1175 Gomberg, J., P. Bodin, and P. A. Reasenberg (2003). Observing earthquakes triggered in the
1176 near field by dynamic deformations, B. Seismol. Soc. Am., 93, 118-138.

1177 Got, J.L., Fréchet, J. and Klein, F.W., 1994. Deep fault plane geometry inferred from
1178 multiplet relative relocation beneath the south flank of Kilauea. Journal of Geophysical
1179 Research: Solid Earth, 99(B8), pp.15375-15386.

1180 Griggs, D. T. and J. D. Blacic, 1965, Quartz-anomalous weakness of synthetic crystal,
1181 Science, 147, 292–295.

1182 Harris RA (1998) Introduction to special section: Stress triggers, stress shadows and
1183 implications for seismic hazard. Journal of Geophysical Research 103: 24 347–24 358.

1184 Hazarika, P. and Kumar, M.R., 2012. Seismicity and source parameters of moderate
1185 earthquakes in Sikkim Himalaya. Natural hazards, 62(3), pp.937-952.

1186 Hessami, K., Jamali, F., Tabassi, H., 2003b. Map of Major Active Faults of Iran. International
1187 Institute of Earthquake Engineering and Seismology.

1188 Hessami, K., Pantosi, D., Tabassi, H., Shabanian, E., Abbassi, M.-R., Feghhi, K., Solaymani,
1189 S., 2003a. Paleoearthquakes and slip rates of the North Tabriz fault, NW Iran: preliminary
1190 results. Ann. Geophys. 46, 903–915.

1191 Hinze, W. J., L. W. Braile, G. R. Keller, and E. G. Lidiak, 1988, Models for mid-continent
1192 tectonism: An update, *Rev. Geophys.*, **26**, 699–717.

1193 Hosseini, H., Pakzad, M., Naserieh, S., 2019, Iranian Regional Centroid Moment Tensor
1194 Catalog: Solutions for 2012-2017. Physics of the Earth and Planetary Interiors 286: 29-41.

1195 Iio, Y. and Y. Kobayashi, 2002, A physical understanding of large intraplate earthquakes,
1196 Earth Planets Space, 54, 1001–1004.

1197 Irmak, T.S., Yavuz, E., Doğan, B., Akçay, D., Sertçelik, F., 2022, Doğu Anadolu'nun
1198 Sismotektoniği (Seismotectonics of the Eastern Anatolia), AFAD Project No: AFAD-UDAP-
1199 G-20-07, 131 pages, Unpublished Technical Report (in Turkish).

1200 ISC, 2022, International Seismological Centre (ISC), On-line
1201 Bulletin, https://doi.org/10.31905/D808B830.

1202 Jackson, J., 1992. Partitioning of strike-slip and convergent motion between Eurasia and
1203 Arabia in Eastern Turkey and the Caucasus. J. Geophys. Res. 97, 12471–12479.

1204 Jackson, J., McKenzie, D., 1984. Active tectonics of the Alpine–Himalayan Belt between
1205 western Turkey and Pakistan. Geophys. J. R. Astron. Soc. 77 (1), 185–264.

1206 Jackson, J., Priestley, K., Allen, M., Berberian, M., 2002. Active tectonics of the South
1207 Caspian Basin. Geophys. J. Int. 148, 214–245.

1208 Jackson, J.A., Ambraseys, N.N., 1997. Convergence between Eurasia and Arabia in eastern
1209 Turkey and the Caucasus. In: Giardini, D., Balassanian, S. (Eds.), Historical and Prehistorical
1210 Earthquakes in the Caucasus. Kluwer Academic Publishers, Dordrecht, pp. 79–90.

1211 Jeffreys, H., and Bullen, K. E. (1958). Seismological tables-British Association for the
1212 advancement of Science, London. Google Scholar.

1213 Johnston, A. C. and L. R. Kanter, 1990, Earthquakes in stable continental crust, *Sci. Am.*, **262**
1214 (3), 68–75.

1215 Jordan, T.H., Chen, Y.-T., Gasparini, P., Madariaga, R., Main, I., Marzocchi, W.,
1216 Papadopoulos, G., Sobolev, G., Yamaoka, K., Zschau, J., 2011. Operational earthquake
1217 forecasting: state of knowledge and guidelines for utilization, final report by the international
1218 commission on earthquake forecasting for civil protection (ICEF). Ann. Geophys. (54) 4.
1219 https://doi.org/10.4401/ag-5350.

1220 Kagan, Y.Y., Jackson, D.D., 1991. Long-term earthquake clustering. Geophys. J. Int. 104,
1221 117–133.

1222 Kalafat, D., Gürbüz, C. and Üçer, S.B., 1987. Batı Türkiye'de kabuk ve üst manto yapısının
1223 araştırılması. Deprem Araştırma Bülteni, 59, pp.43-64.

1224 Karakhanian, A.S., Trifonov, V.G., Philip, H., Avagyan, A., Hessami, K., Jamali, F.,
1225 Bayraktutan, M.S., Bagdassarian, H., Arakelian, S., Davtyan, V., Adilkhanyan, A., 2004.
1226 Active faulting and natural hazards in Armenia, eastern Turkey and Northern Iran.
1227 Tectonophysics 380, 189–219.

1228 Kenner, S. and P. Segall, 2000. A mechanical model for intraplate earthquakes: Application to
1229 the New Madrid, *Science*, **289**, 2329-2332.

1230 Kikuchi M, Nakamura M, Yoshikawa K (2003). Source rupture processes of the 1944
1231 Tonankai earthquake and the 1945 Mikawa earthquake derived from low-gain seismograms.
1232 Earth Planets Space, 55, 159-172.

1233 Kikuchi, M. and Kanamori, H., 1991. Inversion of complex body waves-III. Bulletin of the
1234 Seismological Society of America, 81(6), pp.2335-2350.

1235 King GCP, Stein RS, Lin J (1994). Static stress changes and the triggering of earthquakes,
1236 Bull Seism Soc Am 84, 935-953.

1237 Koketsu, K. (1985), The extended reflectivity method for synthetic nearfield seismograms, J.
1238 Phys. Earth, 33, 121– 131.

1239 KOERI, 2020, 16 Şubat 2020 Kaşkol-Başkale-Van Depremi Basın Bülteni. Boğaziçi
1240 Üniversitesi, Kandilli Rasathanesi ve Deprem Araştırma Enstitüsü, Bölgesel Deprem-
1241 Tsunami İzleme ve Değerlendirme Merkezi (in Turkish).

1242 Koulakov, I., I. Zabelina, I. Amanatashvili, and V. Meskhia, 2012, Nature of orogenesis and
1243 volcanism in the Caucasus region based on results of regional tomography, Solid Earth, 3(2),
1244 327-337, doi:10.5194/se-3-327-2012.

1245 Lee, W.H.K. and Lahr, J.C., 1972. HYPO71: A computer program for determining
1246 hypocenter, magnitude, and first motion pattern of local earthquakes (p. 100). US Department
1247 of the Interior, Geological Survey, National Center for Earthquake Research.

1248 Lin, J., and Stein, R.S., 2004. Stress triggering in thrust and subduction earthquakes and stress
1249 interaction between the southern San Andreas and nearby thrust and strike-slip faults. J
1250 Geophys Res Vol 109:B02303. https://doi.org/10.1029/2003JB002607

1251 Liu, C. C., A. T. Linde, and I. S. Sacks (2009). Slow earthquakes triggered by typhoons,
1252 Nature, 459, 833-836.

1253 Liu, L. and Zoback, M.D., 1997. Lithospheric strength and intraplate seismicity in the New
1254 Madrid seismic zone, *Tectonics*, **16**, 585–595.

1255 Mahatsente, R., Önal, G., and Çemen, I., (2018), Lithospheric structure and the isostatic state
1256 of Eastern Anatolia: Insight from gravity data modelling. Lithosphere, 10, 279-290.
1257 https://doi.org/10.1130/L685.1.

1258 Masson, F., Djamour, Y., van Gorp, S., Chéry, J., Tatar, M., Tavakoli, F., Nankali, H.,
1259 Vernant, P., 2006. Extension in NW Iran driven by motion of the South Caspian Basin. Earth
1260 Planet. Sci. Lett. 252, 180–188.

1261 McQuarrie, N., Stock J.M, Verdel, C., Wernicke, B.P., (2003) Cenozoic evolution of
1262 Neotethys and implications for the causes of plate motions. Geophys Res Lett 30: 2036.
1263 doi:10.1029/2003GL017992.

1264 Mercier, J. L., Carey-Gailhardis, E., Sebrier, M., 1991. Paleostress determinations from fault
1265 kinematics: application to the neotectonics of the Himalayan-Tibet and the central Andes.
1266 Philos. Trans. R. Soc. Lond. Ser. A 337, 41-52.

1267 Mesbahi, F., Bakhti, K., 2020. Kharvana–Zonouz Active Fault System: An Evidence of
1268 Transpressional Tectonic Regime, North-West of Iran, ISSN 0016-8521, Geotectonics, Vol.
1269 54, No. 5, pp. 679-690.

1270 Mohammad R. G., Mohammad R. Sheikholeslami, Hamid R. Javadi, G., Heidarzadeh, 2023,
1271 Block rotation, kinematic relations, and block configurations: How do they work in nature?
1272 Journal of Structural Geology, Volume 176, https://doi.org/10.1016/j.jsg.2023.104979

1273 Moradi, A.S., Hatzfeld, D., Tatar, M., 2011, Microseismicity and seismotectonics of the north
1274 Tabriz fault (Iran), Tectonophysics, vol. 506, nos. 1–4, pp. 22–30.

1275 MTA, 2022, Maden Tetkik ve Arama Enstitüsü (General Directorate of Mineral Research and
1276 Exploration) https://www.mta.gov.tr/v3.0/hizmetler/yenilenmis-diri-fay-haritalari (visited on
1277 05.01.2022).

1278 Niassarifard, M., Shabanian, E., Solaymani Azad, S., Madanipour, S. 2021, New tectonic
1279 configuration in NW Iran: Intracontinental dextral shear between NW Iran and SE Anatolia,
1280 Tectonophysics, Volume 811, 228886, ISSN 0040-1951,
1281 https://doi.org/10.1016/j.tecto.2021.228886.

1282 Nilforoushan, F., Masson, F., Vernant, P., Vigny, C., Martinod, J., Abbassi, M.-R., Nankali,
1283 H., Hatzfeld, D., Bayer, R., Tavakoli, F., Ashtiani, M., Doerflinger, E., Daignières, M.,
1284 Collard, P., Chéry, J., 2003. GPS network monitors the Arabia–Eurasia collision deformation
1285 in Iran. J. Geod. 77, 411–422.

1286 Okada Y (1992) Internal deformation due to shear and tensile faults in a half-space. Bull
1287 Seism Soc Am 82, 1018-1040.

1288 Örgülü, G., Aktar, M., Türkelli, N., Sandvol, E., and Barazangi, M., 2003, Contribution to the
1289 seismotectonics of eastern Turkey from moderate and small size events: Geophysical
1290 Research Letters, v. 30, p. 8040, doi: 10.1029/2003GL018258.

1291 Peyret M, Rolandone F, Dominguez S, Djamour Y, Meyer B (2008) Source model for the Mw
1292 6.1, 31 March 2006, Chalan-Chulan earthquake (Iran) from InSAR. Terra Nova 20: 126–133.

1293 Raleigh, C.B., Healy, J.H., Bredehoeft, J.D., et al., 1972. Faulting and crustal stress at
1294 rangely, Colorado. In: Heard, H.C. (Ed.), Flow and Fracture of Rocks, Geophys. Monogr.
1295 Ser., vol. 16. AGU, Washington, D.C, pp. 275–284.

1296 Reid, M.R., Delph, J.R., Cosca, M.A., Schleiffarth, W.H., and Kuşcu, G.G., 2019, Melt
1297 equilibration depths as sensors of lithospheric thickness during Eurasia-Arabia collision and
1298 the uplift of the Anatolian Plateau: Geology, v. 47, https://doi.org/10.1130/G46420.1.

1299 Reilinger, R.E., McClusky, S., Vernant, P., Lawrence, S., Ergintav, S., Cakmak, R., Ozener,
1300 H., Kadirov, F., Guliev, I., Stepanyan, R., Nadariya, M., Hahubia, G., Mahmoud, S., Sakr, K.,
1301 ArRajehi, A., Paradissis, D., Al-Aydrus, A., Prilepin, M., Guseva, T., Evren, E., Dimitrotsa,
1302 A., Filikov, S.V., Gomez, F., Al-Ghazzi, R., Karam, G., 2006. GPS constraints on continental
1303 deformation in the Africa–Arabia–Eurasia continental collision zone and implications for the
1304 dynamics of plate interactions. J. Geophys. Res. 111, B05411.
1305 http://dx.doi.org/10.1029/2005JB004051.

1306 Rezapour, M., 2024, Aftershock Analyses of the Qotur Doublet-Earthquakes on 23 February
1307 2020 in West-Azarbaijan Province, NW-Iran. Pure Appl. Geophys. 181, 37–52.
1308 https://doi.org/10.1007/s00024-023-03406-8.

1309 Rizza, M., Vernant, P., Ritz, J. F., Peyret, M., Nankali, H., Nazari, H., Masson, F. (2013).
1310 Morphotectonic and geodetic evidence for a constant slip-rate over the last 45 kyr along the
1311 Tabriz Fault (Iran). Geophysical Journal International, 193 (3), 1083-1094.
1312 https://doi.org/10.1093/gji/ggt041.

1313 Rolland, Y., 2017, Caucasus collisional history: Review of data from East Anatolia to West
1314 Iran. Gondwana Research 49, 130-146, http://dx.doi.org/10.1016/j.gr.2017.05.005.

Salmanian, M., Rastbood, A., Hossainali, M. M., 2025, Evaluating interseismic deformation patterns in the North Tabriz Fault (Iran) using enhanced fitting of velocity field and analysis of surface deformation, Journal of Asian Earth Sciences, Volume 277, https://doi.org/10.1016/j.jseaes.2024.106376.

Sandwell, D., R.. Mellors, X. Tong, M. Wei, and P. Wessel (2011), Open radar interferometry software for mapping surface deformation, Eos Trans. AGU, 92(28), doi:10.1029/2011EO280002.

Sandwell, D., Mellors, R., Tong, X., Xu, X., Wei, M., Wessel, P., 2016, GMTSAR: An InSAR Processing System Based on Generic Mapping Tools. UC San Diego: Scripps Institution of Oceanography. Retrieved from: http://topex.ucsd.edu/gmtsar/tar/GMTSAR_2ND_TEX.pdf

Sarkarinejad, K., Faghih, A., Grasemann, B., 2008, Transpressional deformations within the Sanandaj-Sirjan metamorphic belt (Zagros Mountains, Iran), J. Struct. Geol. **30**, 818–826.

Sepahvand, M.R., Yaminifard, F., Tatar, M., Abbassi, M.R., 2012, Aftershocks study of the 2006 Silakhur earthquake (Zagros, Iran): seismological evidences for a pull-apart basin along the Main Recent Fault, Doroud segments, J Seismol, 16: 233–251, doi: 10.1007/s10950-011-9266-3.

Shirzad, T., Ravesh, V. S., Mortezanejad, G., Abdollahi, S., Kazemnia, M. K., Naghavi, M., Rahimi, H., Hatami, M. R., 2024, The crustal and upper-mantle structure beneath NW Iran: an integrated analysis of surface waves and gravity data, Geophysical Journal International, Volume 239, Issue 2, Pages 982–999, https://doi.org/10.1093/gji/ggae306.

Siahkali Moradi, A., 2008. Seismicity–Seismotectonic and Velocity Structure of the Earth's Crust within the Bam and Tabriz Strike-slip Fault Zones (PhD thesis) International Institute of Earthquake Engineering and Seismology (IIEES).

Siahkali Moradi, A., Hatzfeld, D., Tatar, M., 2011. Microseismicity and seismotectonics of the North Tabriz fault (Iran). Tectonophysics 506, 22–30.

Sibson, R. H., 1985. A note on fault reactivation, J. Struct. Geol., 7: 751-754.

Sibson, R.H., 1989. Earthquake faulting as a structural process. J. Struct. Geol. 11, 1–14.

1343 Skobeltsyn, G., Mellors, R., Gök, R., Türkelli, N., Yetirmishli, G., and Sandvol, E., 2014,
1344 Upper mantle *S* wave velocity structure of the East Anatolian-Caucasus region: Tectonics, v.
1345 33, p. 207-221, doi: 10.1002/2013TC003334.

1346 Sokos, E. and Zahradník, J., 2013. Evaluating centroid-moment-tensor uncertainty in the new
1347 version of ISOLA software. Seismological Research Letters, 84(4), pp.656-665.

1348 Sokos, E.N. and Zahradnik, J., 2008. ISOLA a Fortran code and a Matlab GUI to perform
1349 multiple-point source inversion of seismic data. Computers & Geosciences, 34(8), pp.967-
1350 977.

1351 Solaymani Azad, S., Dominguez, S., Philip, H., Hessami, K., Foroutan, M., Shahpasand
1352 Zadeh, M., Ritz, J.-F., 2011. The Zandjan fault system: morphological and tectonic evidence
1353 of a new active fault network in the NW of Iran. Tectonophysics 506, 73–85.

1354 Solaymani Azad, S., Philip, H., Dominguez, S., Hessami, K., Shahpasandzadeh, M.,
1355 Foroutan, M., Tabassi, H., Lamothe, M., 2015, Paleoseismological and morphological
1356 evidence of slip rate variations along the North Tabriz fault (NW-Iran), Tectonophysics 640-
1357 641, 20-38. https://dx.doi.org/10.1016/j.tecto.2014.11.010.

1358 Solaymani Azad, S., Nemati, M., Abbassi, M.-R., Foroutan, M., Hessami, K., Dominguez, S.,
1359 et al., 2019, Active-couple indentation in geodynamics of NNW Iran: Evidence from
1360 synchronous left- and right-lateral co-linear seismogenic faults in western Alborz and Iranian
1361 Azerbaijan domains. Tectonophysics, 754, 1–17. https://doi.org/10.1016/j.tecto.2019.01.013.

1362 Stein, R. S., G. C. P. King, and J. Lin, 1992. Change in failure stress on the southern San
1363 Andreas fault system caused by the 1992 Magnitude=7.4 Landers earthquake, Science, 258,
1364 1328-1332.

1365 Stein, R. S., Lisowski, M., 1983, The 1979 homestead valley earthquake sequence, California:
1366 Control of aftershocks and postseismic deformation, J. Geophys. Res., vol. 88, no. B8, pp.
1367 6477-6490.

1368 Stein, R.S., (1999). The role of stress in the earthquake occurrence. Nature, 402, 605-609.

1369 Sykes, L. R., 1978, Intraplate seismicity, reactivation of preexisting zones of weakness,
1370 alkaline magmatism, and other tectonism postdating continental fragmentation, *Rev.*
1371 *Geophys.*, **16**, 621–688.

1372 Talebian M, Jackson J (2004) A reappraisal of earthquake focal mechanisms and active
1373 shortening in the Zagros mountains of Iran. Geophys J Int 156: 506–526.

1374 Talebian, M., Jackson, J.A., 2002. Offset on the Main Recent fault of the NW Iran and
1375 implications for the late Cenozoic tectonics of the Arabia–Eurasia collision zone. Geophys. J.
1376 Int. 150, 422–439.

1377 Tapponnier, P., Peltzer, G., Armijo, R., 1986, On the Mechanics of the Collision between
1378 India and Asia. London, U.K.: Geological Society.

1379 Taylor, M. and Peltzer, G., 2006. Current slip rates on conjugate strike-slip faults in central
1380 Tibet using synthetic aperture radar interferometry, *J. geophys. Res.,* **111,** B12402,
1381 doi:10.1029/2005JB004014.

1382 Taymaz, T., Ganas, A., Berberian, M., Eken, T., Irmak, T.S., Kapetanidis, V., Yolsal-
1383 Çevikbilen, S., Erman, C., Keleş, D., Esmaeili, C., Tsironi, V., Özkan, B., 2022, the 23
1384 February 2020 Qotur-Ravian earthquake doublet at the Iranian-Turkish border: Seismological
1385 and InSAR evidence for escape tectonics, Tectonophysics (838), 229482,
1386 https://doi.org/10.1016/j.tecto.2022.229482.

1387 Tchalenko, J. S., M. Berberian, 1974, The Salmas (Iran) earthquake of May 6th, 1930, Ann.
1388 Geofis., 27, 151-212.

1389 Tchalenko, J.S, Braud, J., (1974) Seismicity and structure of the Zagros (Iran)-the main recent
1390 fault between 33 and 35°N. Philos. Trans. R. Soc. Lond. 277: 1-25.

1391 TMMOB, 2020. 23 Şubat 2020 Başkale Depremi Teknik İnceleme Raporu. Türk Mühendisler
1392 ve Mimarlar Odalar Birliği (TMMOB) Van İl Koordinasyon Kurulu (in Turkish),
1393 https://www.tmmob.org.tr/sites/default/files/baskale_depremi_teknik_inceleme_raporu.pdf.

1394 Toda S, Stein R (2003) "Toggling of seismicity by the 1997 Kagoshima earthquake couplet:
1395 A demonstration of time-dependent stress transfer" J Geophys Res 108(B12), 2567,
1396 doi:10.1029/2003JB002527.

1397 Toda, S., R. S. Stein, K. Richards-Dinger, and S. B. Bozkurt (2005). Forecasting the evolution
1398 of seismicity in southern California: Animations built on earthquake stress transfer, J.
1399 Geophys. Res., 110, B05S16, doi: 10.1029/2004jb003415.

1400 Toker, M., Pınar, A., Hoşkan, N., 2021. An integrated critical approach to off-fault strike-slip
1401 motion triggered by the 2011 Van mainshock (*Mw 7.1*), Eastern Anatolia (Turkey): New
1402 stress field constraints on subcrustal deformation. J. Geodyn. 147 (101861),
1403 https://doi.org/10.1016/j.jog.2021.101861.

1404 Toker, M., Pınar, A., Tur, H., 2017b. Source mechanisms and faulting analysis of the
1405 aftershocks in the Lake Erçek area (Eastern Anatolia, Turkey) during the 2011 Van event
1406 (Mw 7.1): implications for the regional stress field and ongoing deformation processes. J.
1407 Asian Earth Sci. 150, 73–86.

1408 Toker, M., Şahin, S., 2019. Crustal Poisson's ratio tomography and velocity modeling across
1409 tectono-magmatic lake regions of Eastern Anatolia (Turkey): new geophysical constraints for
1410 crustal tectonics. J. Geodyn. 131 (101651), 1–28. https://doi.org/ 10.1016/j.jog.2019.101651.

1411 Toker, M., Şengör, A.M.C., Demirel-Schluter, F., Demirbağ, E., Çukur, D., Imren, C.,
1412 Niessen, F., Group, P.-W., 2017a. The structural elements and tectonics of the Lake Van basin
1413 (Eastern Anatolia) from multi-channel seismic reflection profiles. J. Afr. Earth Sci. 129, 165–
1414 178.

1415 Toker, M., Tur, H., 2018. Structural patterns of the Lake Erçek Basin, eastern Anatolia
1416 (Turkey): evidence from single-channel seismic interpretation. Mar. Geophys. Res.
1417 https://doi.org/10.1007/s11001-017-9333-4.

1418 Toker, M., Tur, H., 2021. Shallow seismic characteristics and distribution of gas in lacustrine
1419 sediments at Lake Erçek, Eastern Anatolia, Turkey, from high-resolution seismic data.
1420 Environ Earth Sci 80, 727, https://doi.org/10.1007/s12665-021-10039-4.

1421 Toker, M., Şahin, Ş., 2022. Upper- to mid-crustal seismic attenuation structure above the
1422 mantle wedge in East Anatolia, Turkey: Imaging crustal scale segmentation and
1423 differentiation, Physics of the Earth and Planetary Interiors.
1424 https://doi.org/10.1016/j.pepi.2022.106908.

1425 Toker, M., Pınar, A., 2024, New strain configuration of convergence in the Arabia-Eurasia
1426 collisional zone: A comprehensive analysis of large shear zones inferred from geodetic and
1427 seismic observations, Journal of Asian Earth Sciences 271 (2024) 106235,
1428 https://doi.org/10.1016/j.jseaes.2024.106235

1429 Topuz, G., Candan, O., Zack, T., Yilmaz, A., 2017. East Anatolian plateau constructed over a
1430 continental basement: No evidence for the East Anatolian accretionary complex. Geology 45
1431 (9). https://doi.org/10.1130/G39111.1.

1432 Vernant, P., Chéry, J., 2006. Mechanical modelling of oblique convergence in the Zagros,
1433 Iran. Geophys. J. Int. 165, 991–1002.

1434 Vernant, P., Nilforoushan, F., Hatzfeld, D., Abbassi, M.-R., Vigny, C., Masson, F., Nankali,
1435 H., Martinod, J., Ashtiani, A., Bayer, R., Tavakoli, F., Chéry, J., 2004. Contemporary crustal
1436 deformation and plate kinematics in Middle East constrained by GPS measurement in Iran
1437 and northern Oman. Geophys. J. Int. 157, 381-398.

1438 Yesilova, Ç., 2021. Potential geoheritage assessment: Dereiçi Travertines, Baskale, Van (East
1439 Anatolia, Turkey). Manas Journal of Engineering. 9:66-71.

1440 Yesilova, Ç., Gülyüz E., Ci-Rong H., Chuan-Chou S., 2019. Giant tufas of Lake Van record
1441 lake-level fluctuations and climatic changes in eastern Anatolia, Turkey. Palaeogeography,
1442 Palaeoclimatology, Palaeoecology, 533:1-9.

1443 Yesilova, Ç., Güngör-Yesilova, P., Açlan, M., Tsai-Luen, Y., Chuan-Chou, S., 2021. U-Th
1444 ages and facies properties of Edremit travertine/tufas, Van, Eastern Anatolia: implications of
1445 Neotectonic for the region. Geological Quarterly, 65:28.

1446 Yesilova, Ç., 2022. Climatic and tectonic effects on the origin and evolution of the Dereiçi
1447 travertines (the Baskale Basin, Eastern Turkey), and neotectonic implications, Geological
1448 Quarterly, 66:27, doi: http://dx.doi.org/10.7306/gq.1659.

1449 Waldhauser, F., Ellsworth, W.L., 2000. A double-difference earthquake location algorithm:
1450 Method and application to the northern Hayward fault, California. Bulletin of the
1451 Seismological Society of America, 90 (6), pp.1353-1368.

Wessel, P. and Smith, W.H.F., 1998. New, improved version of the Generic Mapping Tools released, EOS, Trans. Am. Geophys. Un., **79,** 579, doi:10.1029/98EO00426.

White, S. H., Bretan, P. G., and Rutter, E. H., 1986. Fault zone reactivation: kinematics and mechanisms. Phil. Trans. Roy. Soc. Lond., A317, 81-97.

Zoback, M.D., W. H. Prescott, and S. W. Kroeger, 1985, Evidence for lower crustal ductile strain localization in southern New York, Nature, 317, 705-707.

Zoback, M.L., 1992. Stress field constraints on intraplate seismicity in eastern North America. J. Geophys. Res. 97 (B8), 11761-11782.

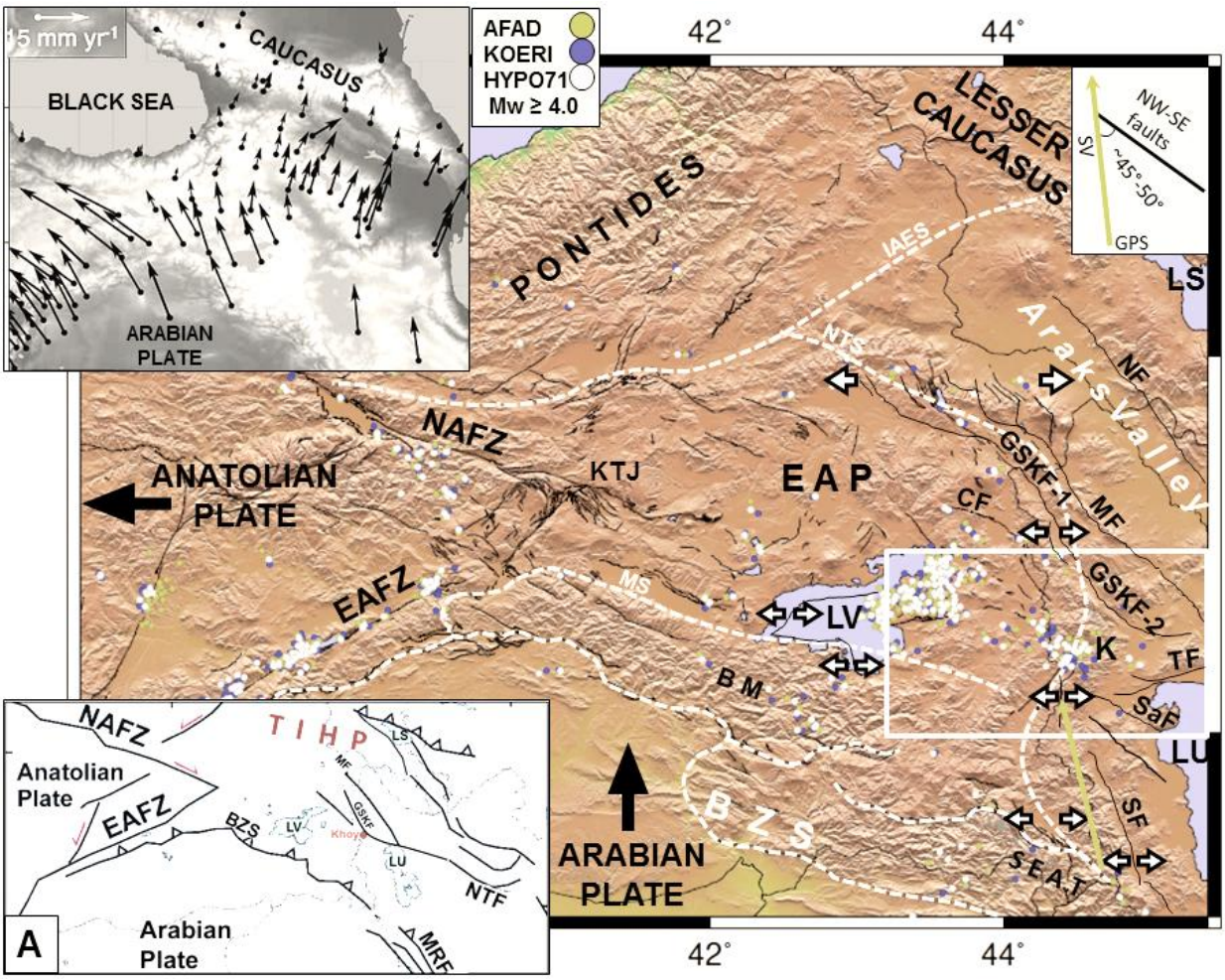
15 mm yr-1
CAUCASUS
BLACK SEA
ARABIAN PLATE
AFAD
KOERI
HYPO71
Mw ≥ 4.0
42°
44°
LESSER CAUCASUS
PONTIDES
NW-SE faults
~45°-50°
SV
GPS
IAES
LS
NTS
NF
Arak-Valley
NAFZ
KTJ
EAP
GSKF-1
CF
MF
ANATOLIAN PLATE
EAFZ
MS
LV
GSKF-2
K
TF
BM
SaF
LU
BZS
SF
SEAT
ARABIAN PLATE
TIHP
Anatolian Plate
Arabian Plate
NTF
MRF
A
42°
44°

1

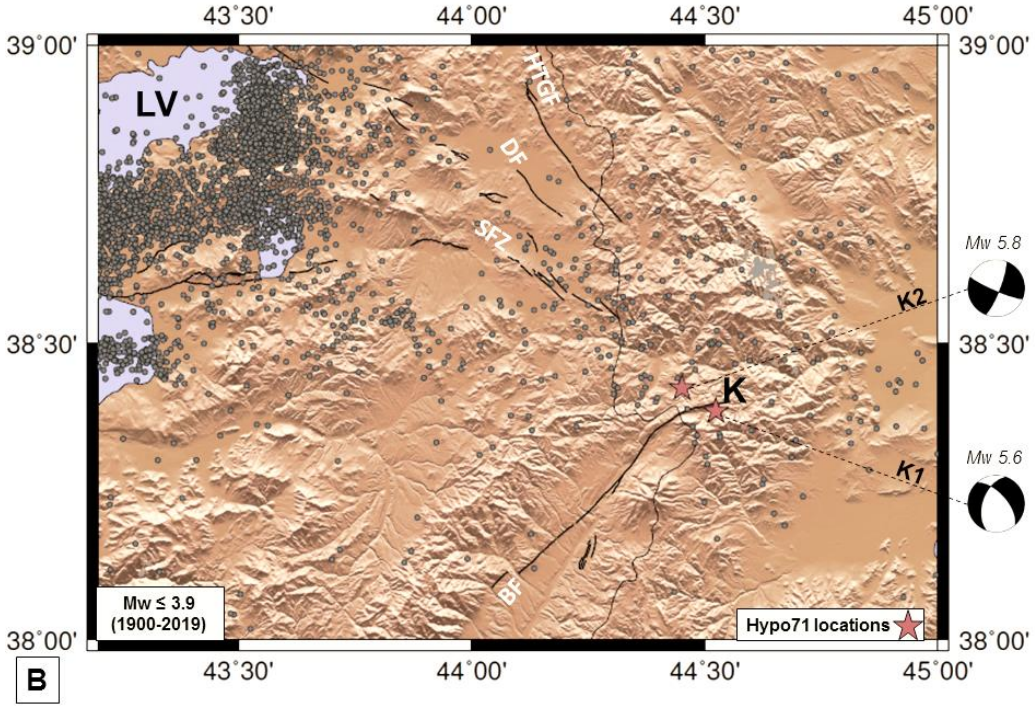
43°30'
44°00'
44°30'
45°00'
39°00'
38°30'
38°00'
LV
HTGF
DF
SF?
Mw 5.8
K2
K
Mw 5.6
K1
BF
Mw ≤ 3.9
(1900-2019)
Hypo71 locations
B

2

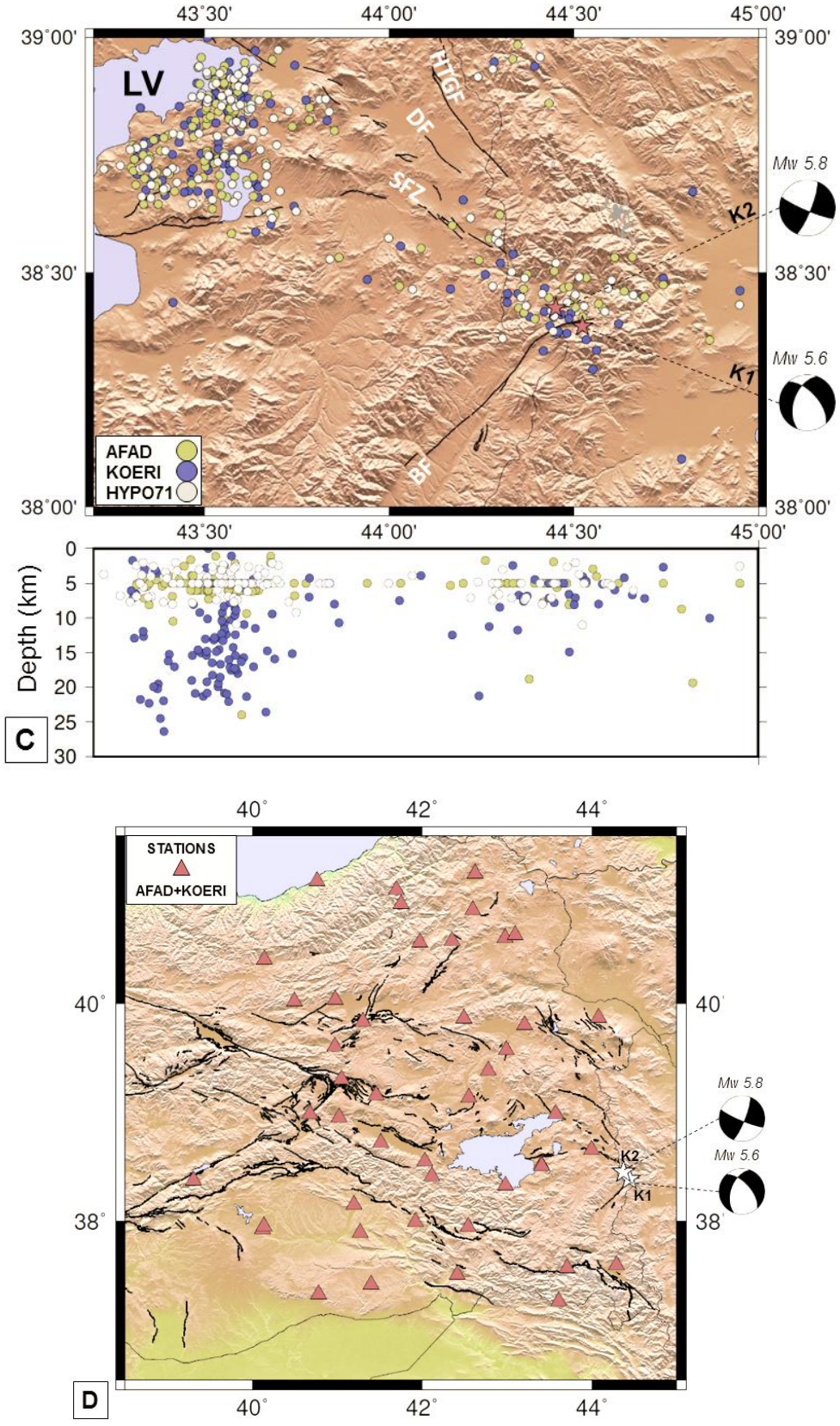
43°30'
44°00'
44°30'
45°00'
39°00'
38°30'
38°00'
LV
HTGF
DF
SFZ
BF
Mw 5.8
K2
Mw 5.6
K1
AFAD
KOERI
HYPO71
Depth (km)
0
5
10
15
20
25
30
C
40°
42°
44°
STATIONS
AFAD+KOERI
D

Figure 1

Figure 1. a. Shaded relief topographic image summarizing the overall seismotectonic structure of E-Anatolia together with NW Iran. Colored circles (top middle) represent initial locations of epicentres of crustal earthquakes (Mw ≥ 4.0, 2010-2022) from the AFAD and KOERI catalogues, and relocations from the Hypo71 catalogue performed in this study. Inset map (top left corner) shows GPS velocity data of Reilinger et al., (2006) relative to Eurasia (taken from Copley and Jackson, 2006). Yellow arrow is the GPS slip vector (SV, ~15 mm/yr) of the border between Turkey-Iran relative to Eurasian plate motion (after Vernant et al., 2004; Djamour et al. 2011; Rolland, 2017), given that the plate convergence angle along the NW-SE trending faults observed and mapped in and along the study area is ~45-50°, consistent with the results of Mesbahi and Bakhti, (2020). The rectangle in white shows the study area and its close surroundings, corresponding to Figs. 1b and c. **b**. Microseismicity (Mw ≤ 3.9, 1900-2019) of the study area and its close surroundings from AFAD and KOERI catalogues. The epicenters of the Khoy-Qotour, Khoy 1 (K1) and Khoy 2 (K2), earthquakes are shown by red stars. Regional centroid moment tensor (CMT) solutions of both events are performed in this study. **c**. Detailed seismicity map (Mw ≥ 4.0, 2010-2022) of the study area and its close surroundings from AFAD, KOERI catalogues and relocation catalogue from Hypo71 in this study. Other details are similar to those of Fig. 1b. **d.** National seismic networks of AFAD (21 stations) and KOERI (25 stations) in E-Anatolia and the vicinity of the study area. Other details are similar to those of Fig. 1b. Regional sutures surrounding E-Anatolia are marked by dashed, curvilinear lines in white (compiled from Topuz et al., 2017). Black lines indicate major active faults of E-Anatolia together with NW-Iran, compiled and digitized from MTA (2022) and also from Djamour et al., (2011), Solaymani Azad et al., (2011, 2015) and Ghods et al., (2015). White arrows indicate the direction of extension in areas inferred from Solaymani Azad et al., (2015) and revised in this study. Black arrows show plate motion directions relative to Eurasia. Abbreviations: TIHP, Turkish-Iranian High Plateau; EAP, East Anatolian Platform; NTF, North Tabriz Fault; MRF, Main Recent Fault; IAES, İzmir-Ankara-Erzincan Suture; NTS, Neo-Tethyan Suture; MS, Mus Suture; BM, Bitlis Massif; BZS, Bitlis Zagros Suture; SEAT, South East Anatolian Thrust; NAFZ, North Anatolian Fault Zone; EAFZ, East Anatolian Fault Zone; KTJ, Karlıova Triple Junction; LV, Lake Van; LU, Lake Urmieh; LS, Lake Sevan; CF, Chalderan Fault; K, Khoy; SF, Serow Fault; SaF, Salmas Fault; TF, Tassuj Fault; GSKF-1, Guilato-Siahcheshmeh-Khoy Fault system-1; GSKF-2, Guilato-

Siahcheshmeh-Khoy Fault system-2; MF, Maku Fault; NF, Nakhichevan Fault; HTGF, Hasan Timur Golu Fault; SFZ, Saray Fault Zone; DF, Dorutay Fault; BF, Baskale Fault.

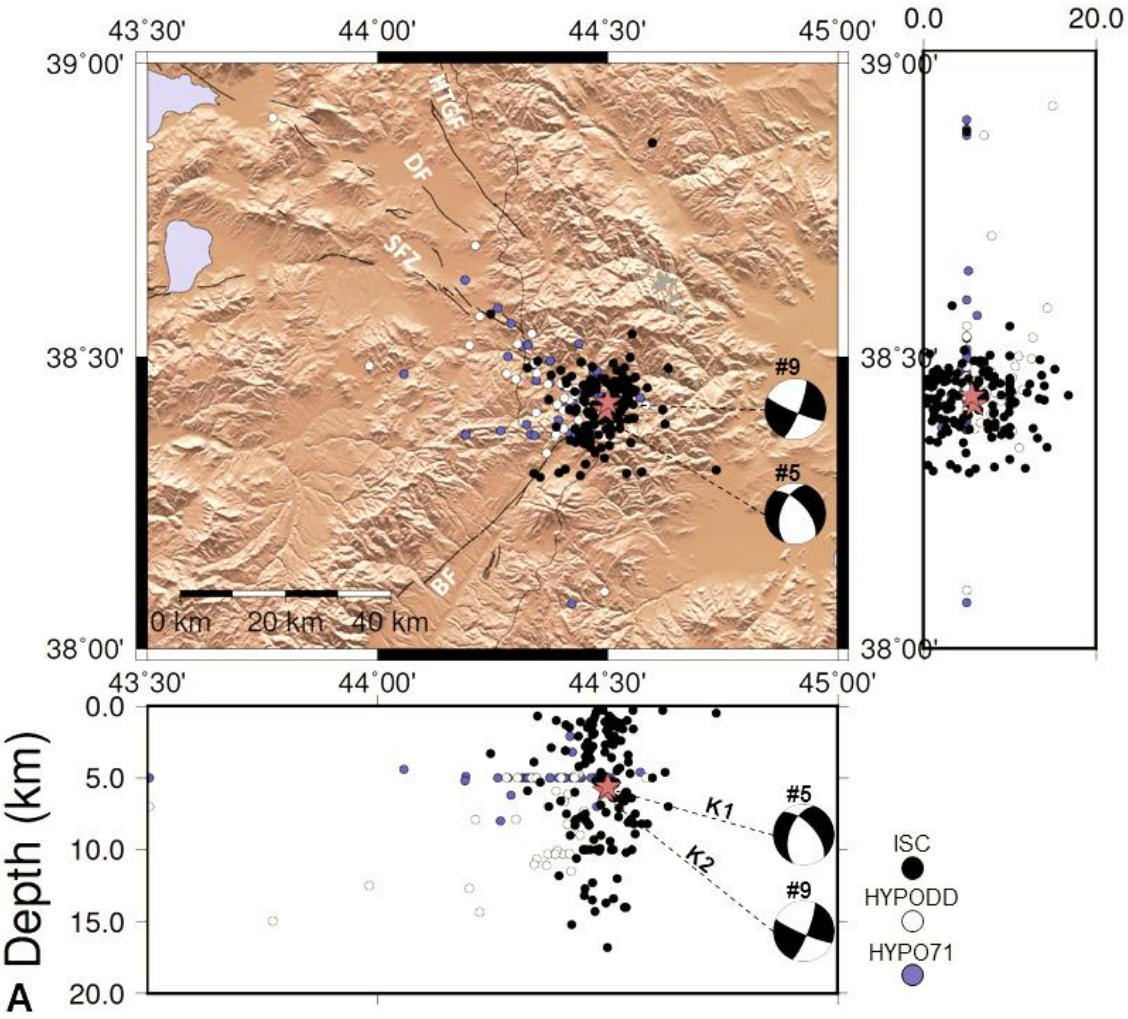
43°30'
44°00'
44°30'
45°00'
39°00'
38°30'
38°00'
0.0
20.0
MTGF
DF
SFZ
BF
#9
#5
0 km
20 km
40 km
Depth (km)
0.0
5.0
10.0
15.0
20.0
K1
K2
ISC
HYPODD
HYPO71
A

67

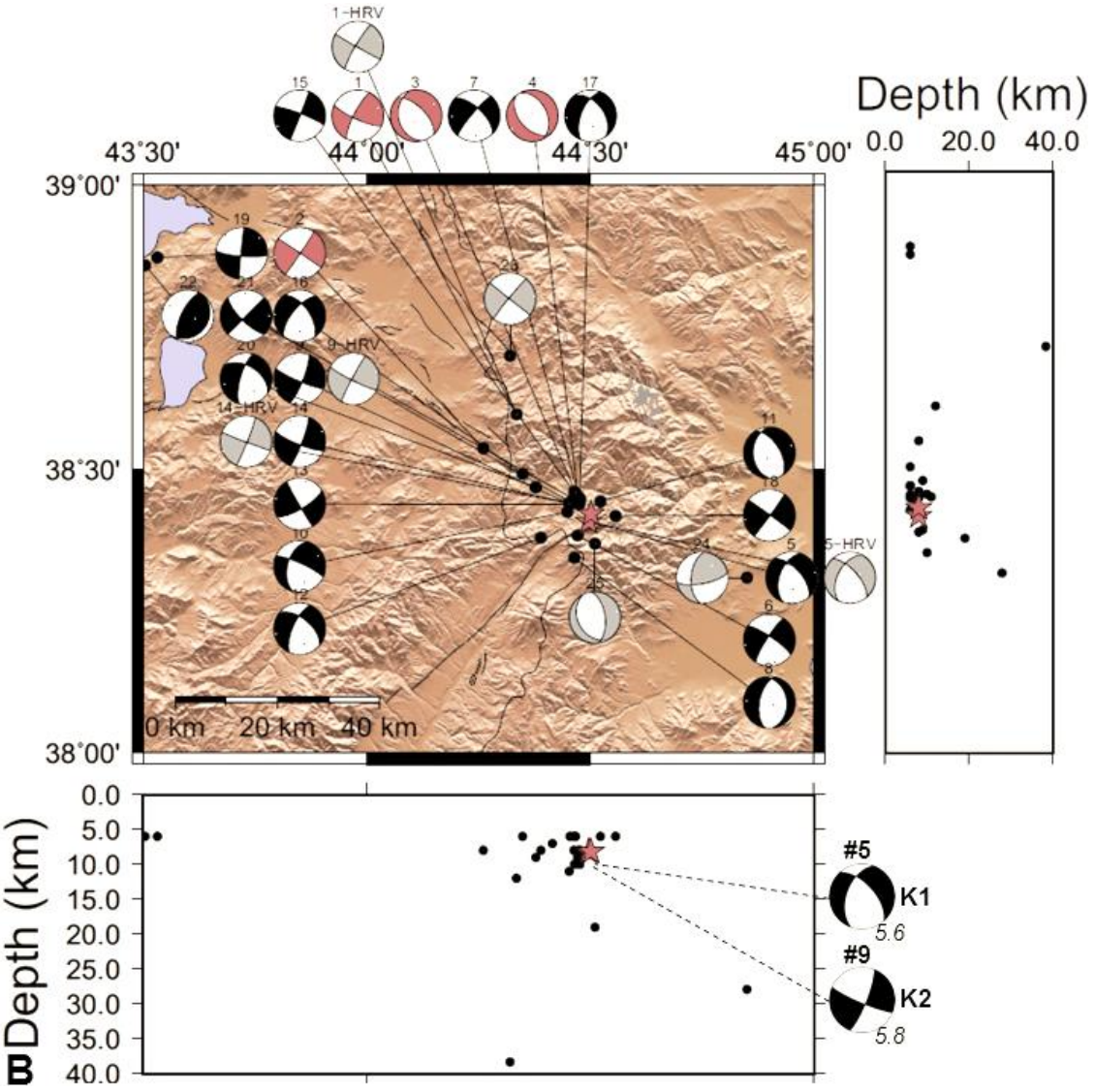

Figure 2

Figure 2. a. Initial locations of mainshocks-aftershock sequence from Hypo71 (before relocation), their relocations from HypoDD (after relocation) and final locations (*Mw* ≥ *3.0*) from the ISC Bulletin, related W-E and N-S cross-sectional depth profiles (see Table S1 for final ISC locations and Fig. S1 for their azimuths). **b.** Focal mechanism solutions from regional CMT inversion and their centroid depths (see Table 2 for fault source parameters). Focal mechanisms in black are from our regional CMT analysis; those in red are the events occurring before K1 and those in grey are the best DC from GCMT solutions for the study area. The four of seven focal mechanisms from GCMT are consistent with our CMT solutions. The number on the top of each focal mechanism gives the number (#) of the events, as labeled in Table 2. The locations of K1

(#5) and K2 (#9) events are shown by red stars (black lines refer to active faults compiled and digitized from MTA, 2022).

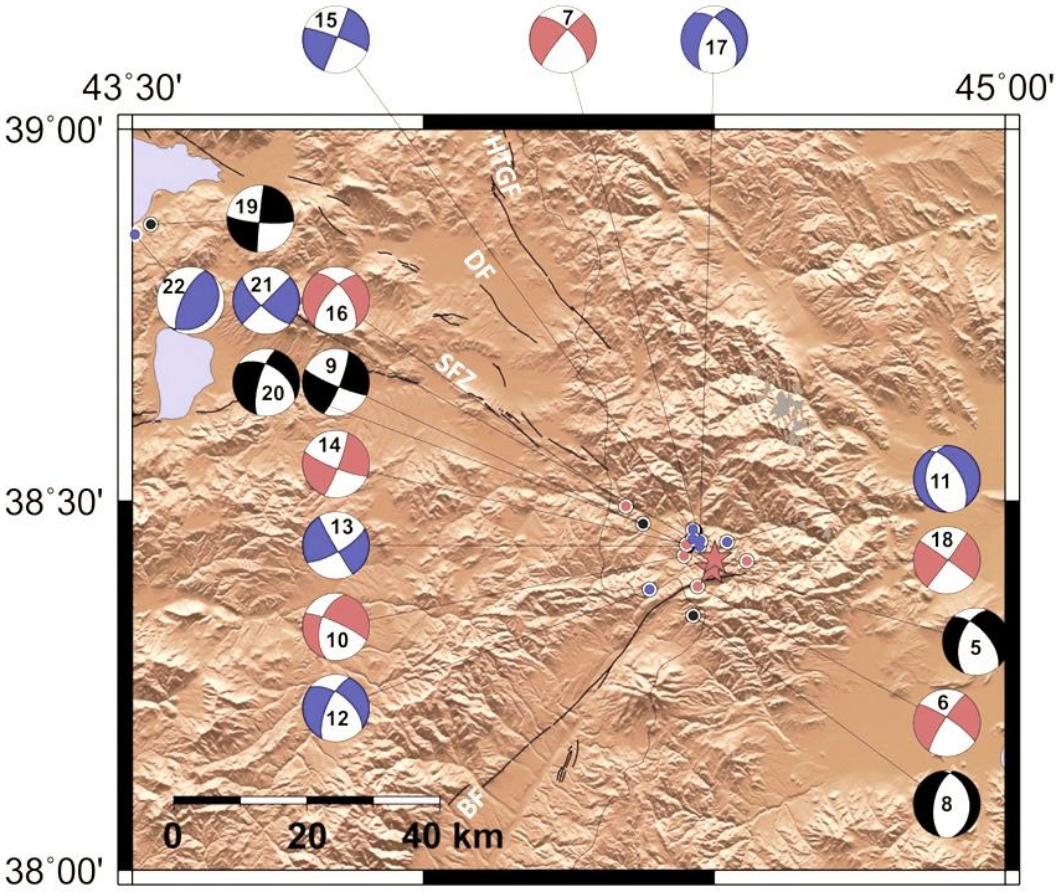

Figure 3

Figure 3. Coulomb failure stress changes of located mainshocks and aftershocks shown in Fig. 2b are illustrated in colored focal patterns of the locations (see Table 2 for source parameters colored in blue and red). Located epicenters and focal patterns in blue refer to negative stress changes (stress decrease); those in red indicate positive stress changes (stress increase), while those in black indicate both positive and negative stress changes (stress increase/decrease or *vice versa*) except for the K1 event (#5). Other details are similar to those of Fig. 2b.

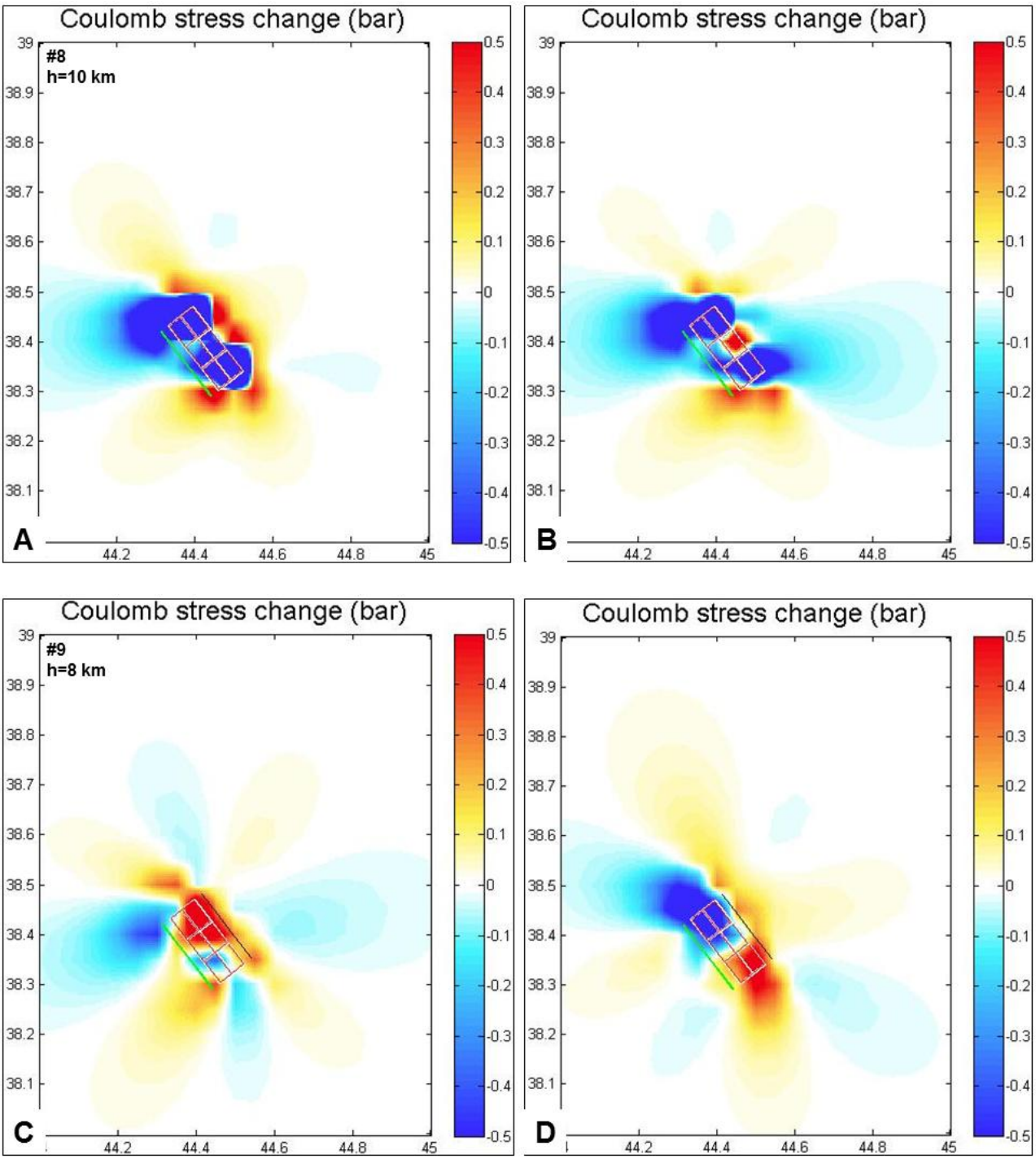

Figure 4

Figure 4. Two distinct samples of co-seismic stress changes estimated in this study. Nodal plane is unloaded in **a** and the other is loaded in **b**, and the nodal plane is loaded in **c**, while the other is unloaded in **d.** Shallow WNW-ESE or nearly W-E trending stress shadow zones (high normal stress) are shown in **a** and **d**. Shallow NW-SE trending stress triggering zones (high shear stress)

are shown in **b** and **c**. Numbers (#) and depths (h) colored in black (top left corners) correspond to locations and focal mechanisms in black shown in Fig. 3 (see Table 2 for details in red/blue).

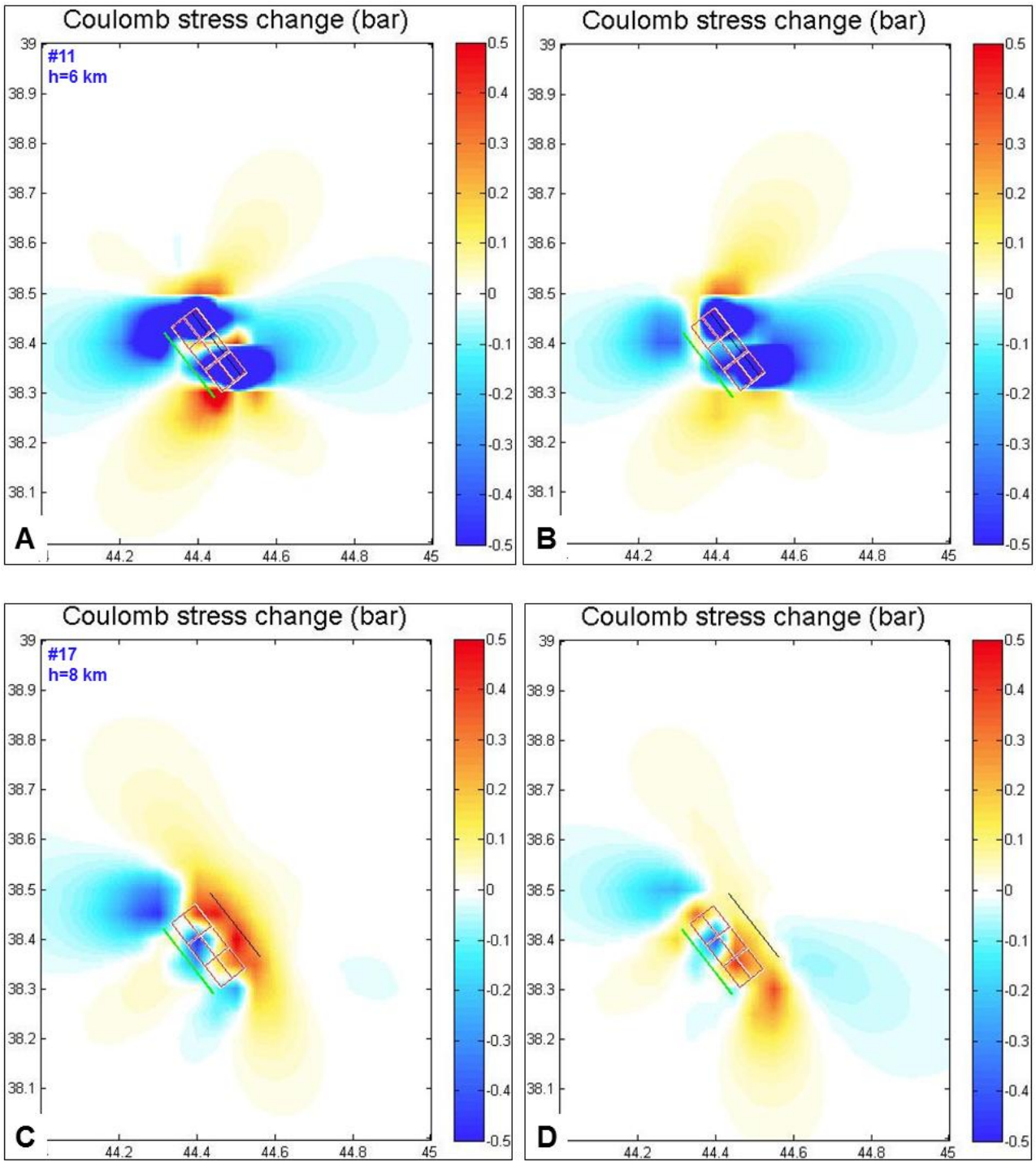

Figure 5

Figure 5. Two samples of co-seismic stress changes estimated in this study. Both nodal planes of nearly N-S striking normal faults are unloaded in **a-d**, indicating shallow WNW-ESE or nearly W-E trending stress shadow zones (high normal stress) from **a** to **d**. Numbers (#) and depths (h)

colored in blue (top left corners) correspond to locations and focal mechanisms in blue shown in Fig. 3 (see Table 2 for details in blue).

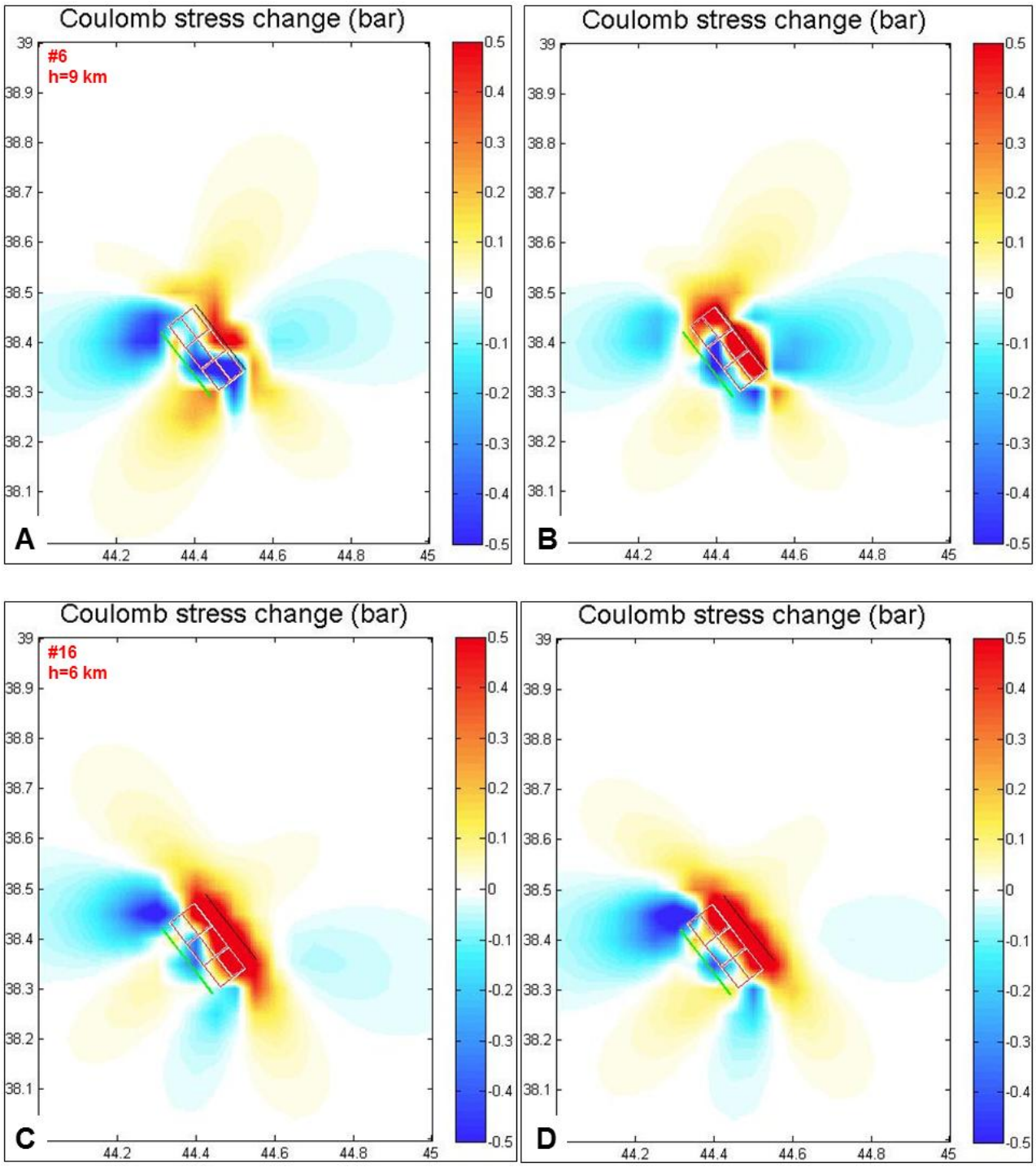

Figure 6

Figure 6. Two samples of co-seismic stress changes estimated in this study. Both nodal planes of nearly NNW-SSE and NW-SE striking right-lateral, moderate to high angle, normal oblique-slip faults are loaded in **a-d**, indicating shallow NW-SE trending stress triggering zones (high shear

stress) from **a** to **d**. Numbers (#) and depths (h) colored in red (top left corners) correspond to locations and focal mechanisms in red shown in Fig. 3 (see Table 2 for details in red).

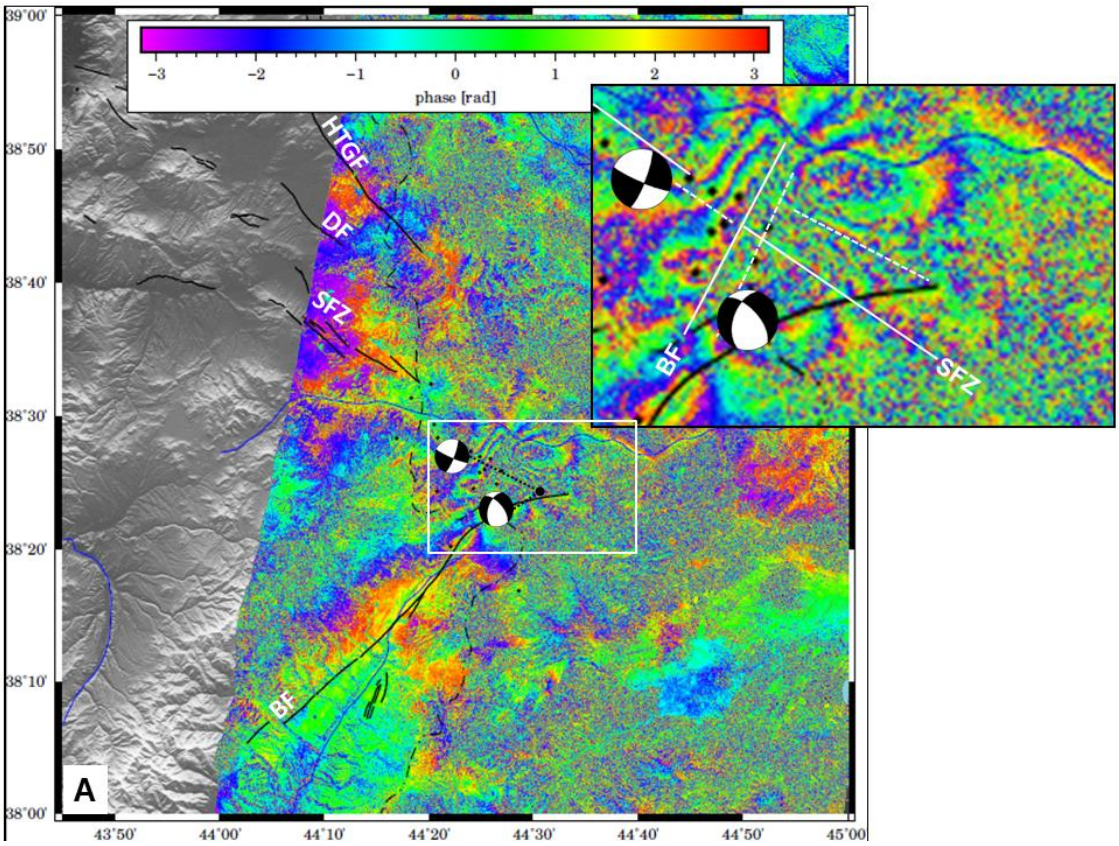
39°00'
38°50'
38°40'
38°30'
38°20'
38°10'
38°00'
43°50'
44°00'
44°10'
44°20'
44°30'
44°40'
44°50'
45°00
−3
−2
−1
0
1
2
3
phase [rad]
HTGF
DF
SFZ
BF
A

217

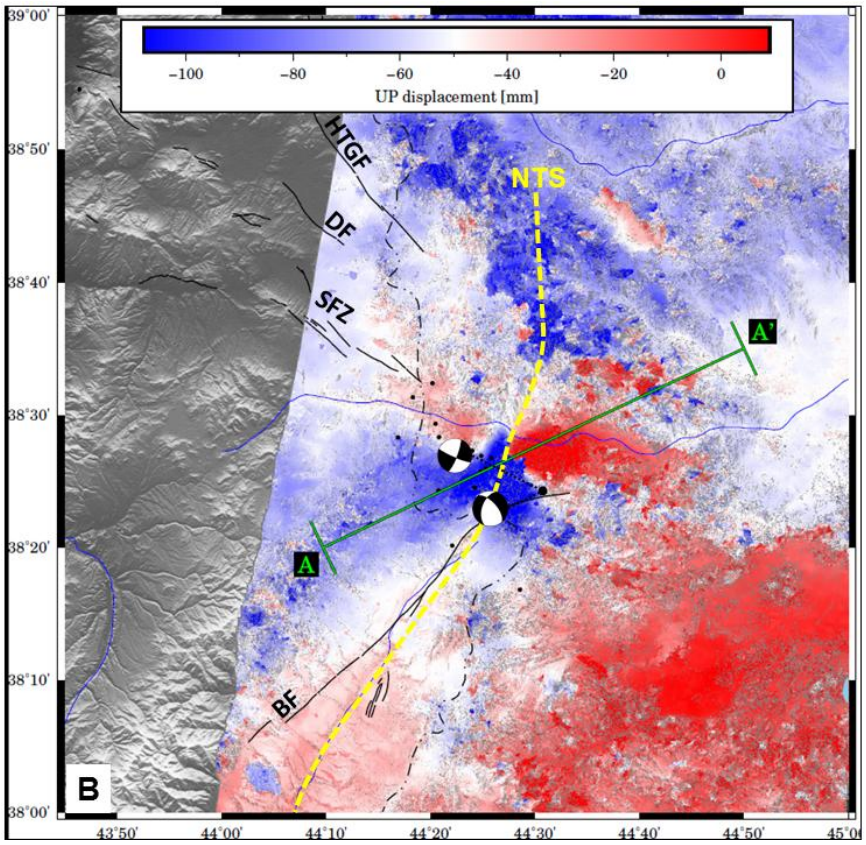
39°00'
38°50'
38°40'
38°30'
38°20'
38°10'
38°00'
43°50'
44°00'
44°10'
44°20'
44°30'
44°40'
44°50'
45°0
−100
−80
−60
−40
−20
0
UP displacement [mm]
HTGF
DF
SFZ
NTS
A'
A
BF
B

218

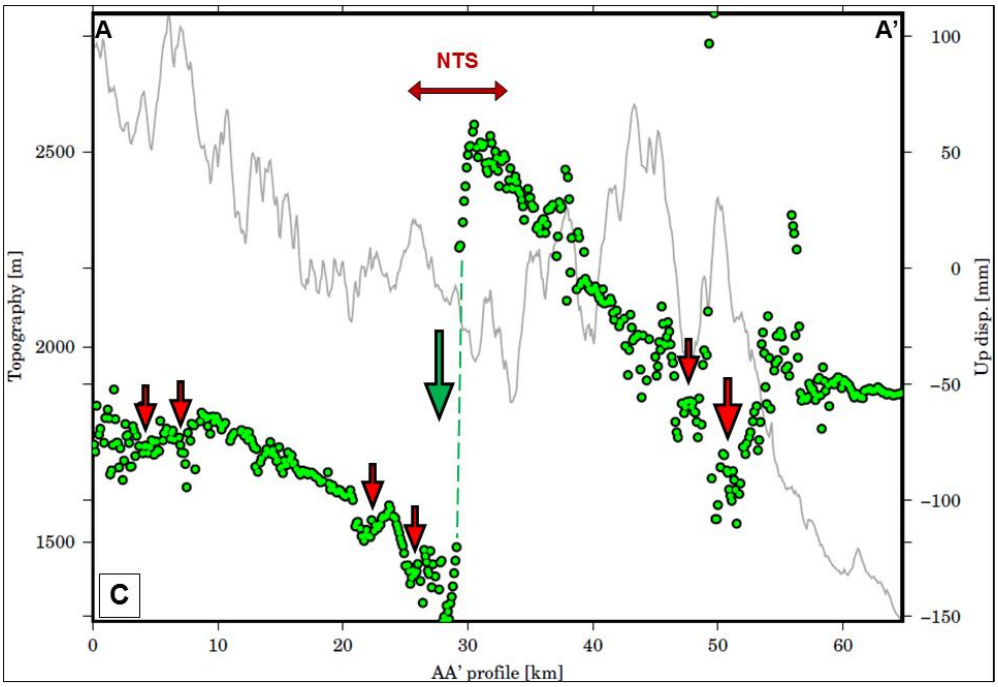

Figure 7

Figure 7. Sentinel 1A SAR images show co-seismic surface deformation patterns of the K1 and K2 events. **a.** S1A_2020053-S1A_2020065 interferogram image (background source from GoogleEarth). The surface ruptures of the K1 and K2 events, shown by a white rectangle, are marked by white lines in relation to the SFZ and BF (inset map). **b**. Vertical surface displacement map for the S1A_2020053-S1A_2020065 interferogram shown in **a**. The NTS zone, striking nearly N-S, is indicated by a curvilinear dashed line in yellow and the A-A' profile is projected on the map. **c**. Cross-sectional A-A' profile of vertical surface displacements (small green dots) in relation to highly irregular topography (grey line) shown in **b** shows a large-scale, block subsidence (green arrow), associated with small-scale vertical fractures (red arrows). The inferred location of the NTS zone, seen in **b,** is indicated by a double-headed arrow (colored brown). Other details are similar to those of Fig. 1.

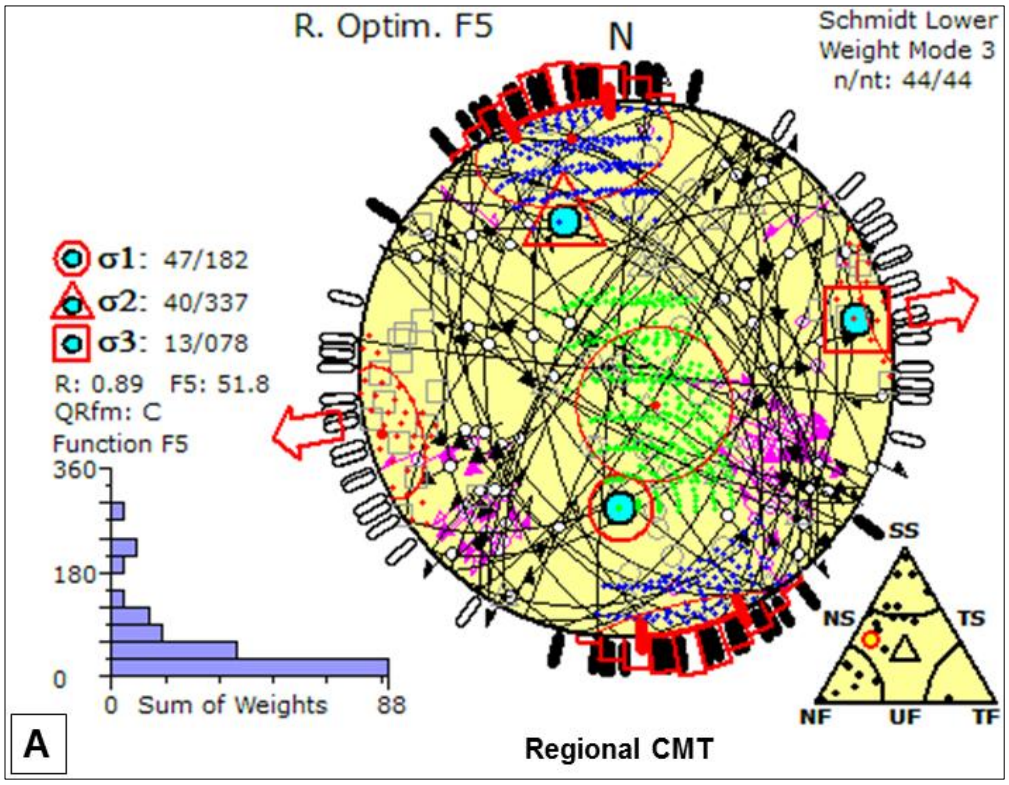

235

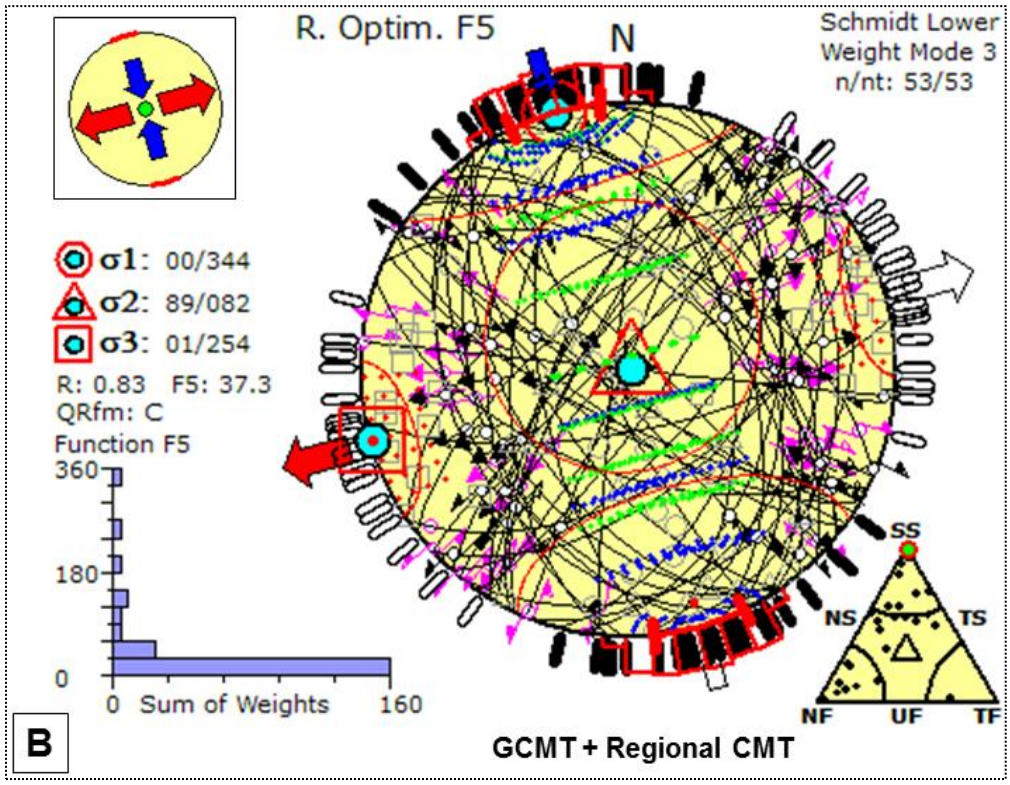

236

237 **Figure 8**

238

Figure 8. Tensor inversion results of regional CMT in **a,** and of regional CMT plus GCMT in **b** (see the text for further details and Fig. 2b for focal mechanisms) are displayed using equal-area stereoplots (lower hemisphere) of the focal planes as a cyclograph trace and related slip lines for normal (black dot with arrow outward), reverse (arrow inward) and strike-slip faulting (double semi-arrows). The orientation of the three principal stress axes (a black dot surrounded by a circle for σ1, a triangle for σ2, and a square for σ3) determines stress inversion results. The large arrows outside the stereogram describe the related S_{Hmax} and S_{Hmin} orientations. The color, type and length of both orientations describe symbolically the horizontal deviational stress magnitude as a function of the isotropic stress (σi), the stress regime and R. Extensional (bσi) and compressional deviating stresses (Nσi) are represented by arrows outwards and inwards, respectively. If σ1, σ2 and σ3 are subhorizontal, the black, green, and white arrows indicate S_{Hmax} (always), S_{Hmin}/S_{Hmax} and S_{Hmin} (always), respectively. The vertical stress (σv) is shaped in a small circle with stress arrows on the top left corner. The σv, indicated by a solid circle, a dot and an open circle, represents extensional (σ1 ≈ σv), strike-slip (σ2 ≈ σv) and compressional regimes (σ3 ≈ σv), respectively. The orientations of the associated kinematic axes are P (in circle), B (in triangle), and T (in square) axes. The histogram on the bottom left corner indicates the distribution of the misfit angle α (SD, Slip. Dev), weighted arithmetically according to the magnitude. The bars outside the stereogram describe the S_{Hmax} (black) and S_{Hmin} (white) directions for individual focal mechanisms and the small gray symbols inside (SS: strike-slip faulting, TS: thrust faulting with strike-slip component, TF: thrust faulting, NF: normal faulting, NS: normal faulting with strike-slip component, and UF: an unknown or oblique stress regime or faulting).

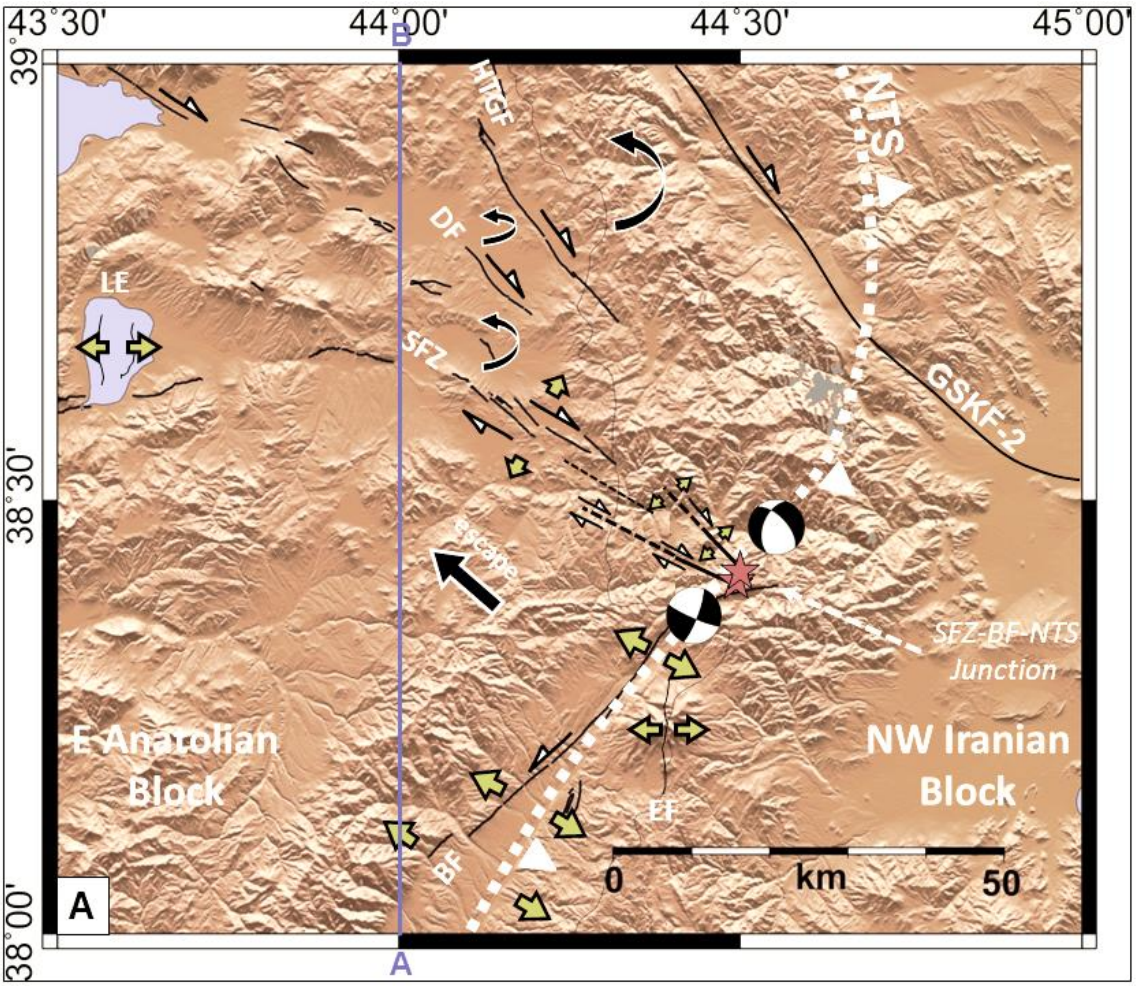
43°30'
44°00'
44°30'
45°00'
39°
38°30'
38°00'
B
A
HTGF
DF
NTS
LE
SFZ
GSKF-2
Escape
SFZ-BF-NTS
Junction
E Anatolian
Block
NW Iranian
Block
EF
BF
0
km
50
A

263

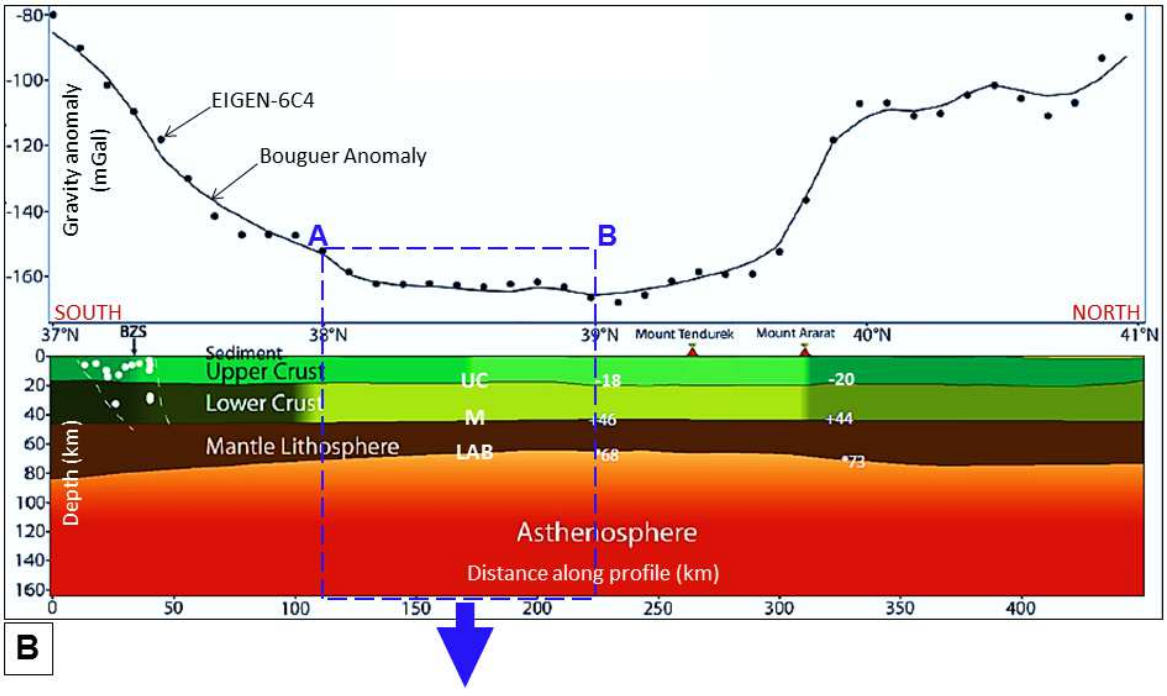
-80
-100
-120
-140
-160
Gravity anomaly
(mGal)
EIGEN-6C4
Bouguer Anomaly
A
B
SOUTH
NORTH
37°N
BZS
38°N
39°N
Mount Tendurek
Mount Ararat
40°N
41°N
Sediment
Upper Crust
Lower Crust
Mantle Lithosphere
UC
M
LAB
-18
-20
+46
+44
+68
+73
Depth (km)
0
20
40
60
80
100
120
140
160
Astheniosphere
Distance along profile (km)
0
50
100
150
200
250
300
350
400
B

264

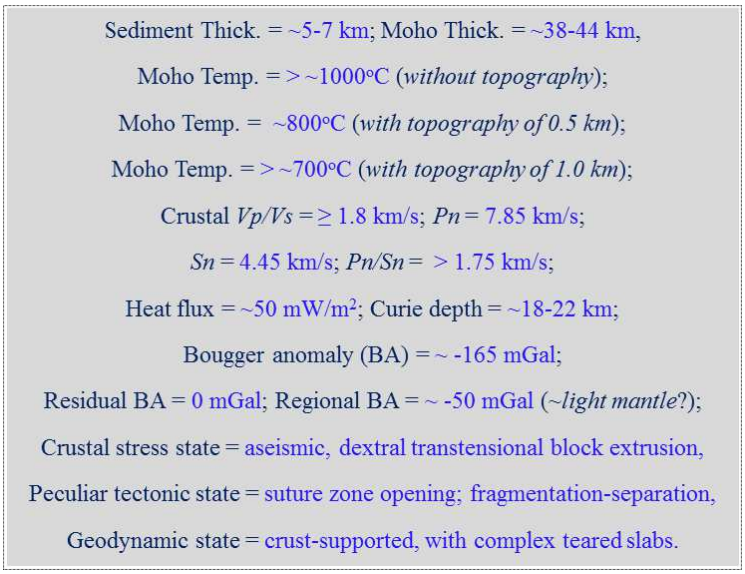

Figure 9

Figure 9. a. Simplified, conceptual tectonic model of the structural setting in the study area together with right-lateral strike-/oblique-slip faults in its close surroundings and conjugate geometry of right-/left-lateral shear pattern (SFZ and BF), as shown in Fig. 1. Based on inferences derived from regional source mechanisms, NNW-SSE striking, nearly N-S striking normal and NW-SE striking right-lateral strike-slip faults ruptured toward SE during K1 and K2 mainshocks (stars in red), respectively, are interpreted and illustrated in an area of rupture source. Dashed black lines are inferred ruptures. Black arrow is an inferred marker to show WNW oblique motion of wedge-shaped extruding block (see A-B profile in blue along 44°E). Arrows in yellow are inferred directions of extensional stress as interpreted from available data and previous studies (Toker et al., 2017a, b; Toker and Tur, 2018). Curved arrows in black are inferred, right-lateral shear block rotations. Note that the NTS strikes parallel/sub-parallel to BF toward the rupture source area (SFZ-BF-NTS junction) and that NTS, BF, SFZ are well consistent with both nodal planes of CMT solutions (LE, Lake Erçek; EF, Extensional Fracture). **b.** The blue thick line projected on the map (A-B profile along 44°E) shows the location of the 2.5-dimensional (2.5-D) gravity model (based on EIGEN-6C4 data) of the study area and its close surroundings (processed gravity data and models of E-Anatolia from Mahatsente et al., 2018). The white circles represent earthquakes (M≥4.2, 1985-2016) from KOERI. The numbers in the model show the lithosphere-asthenosphere boundary (stars in LAB), Moho (crosses in M) and upper crustal depths (negatives in UC) from receiver function and seismic tomography (Angus et al., 2006;

Delph et al., 2015; Mahatsente et al., 2018). The white dashed lines show the inferred location of the BZS. Dashed rectangle in blue shows a cross-section of the A-B profile in the study area and its close surroundings. The thick blue arrow indicates a chart in grey; a compiled list of related geophysical parameters from Artemieva and Shulgin, (2019) associated with the A-B cross-section. Based on compiled geophysical data sets from Mahatsente et al., (2018) and Artemieva and Shulgin, (2019), marked density heterogeneity in the crust and upper mantle and thermal weakening due to a thermally altered crust by asthenospheric underplating (Mahatsente et al., 2018) can be observed in the study area and its close surroundings, where high Moho temperature and high *Vp/Vs* associated with low heat flux, suggest a crustal detachment and aseismic block extrusion in a sense of right-lateral shear.

Supplementary Files

This is a list of supplementary files associated with this preprint. Click to download.

- TablesFinal.docx
- SupplementaryMaterial.docx